The 18S rRNA methyltransferase, BUD23, is required for appropriate lipid and mitochondrial metabolism

Noelia Martinez-Sanchez[1], Anneke Brümmer[2,3], Nichola J. Barron[4], Daniel B. Rosoff[1], Angélica Liechti[2], Maria Voronkov[1,5], Edward A. Hayter[4], Sébastien Chamois[2], René Dreos[2], Nicolas Guex[3], Elspeth Johnson[1], Matthew Baxter[1], Kerri Smith[6], Rebecca C Northeast[4], Gina Galli[6], Leanne Hodson[1], David Gatfield[2#], David W. Ray[1#], David A. Bechtold[4#]

Affiliations

[1] National Institute for Health and Care Research Oxford Health Biomedical Research Centre and John Radcliffe Hospital, Oxford, UK; Oxford Centre for Diabetes, Endocrinology and Metabolism and Oxford Kavli Institute for Nanoscience Discovery, University of Oxford, Oxford, UK.

[2] Center for Integrative Genomics, University of Lausanne, 1015 Lausanne, Switzerland

[3] Bioinformatics Competence Center, University of Lausanne, 1015 Lausanne, Switzerland

[4] Centre for Biological Timing, School of Medical Sciences, Faculty of Biology, Medicine and Health, University of Manchester, Manchester, M13 9PT, UK

[5] Current address: Proteomics Facility, The Francis Crick Institute, London NW1 1AT, UK

[6] Division of Cardiovascular Sciences, School of Medical Sciences, Faculty of Biology, Medicine and Health, University of Manchester, Manchester, M13 9PT, UK

Joint senior and corresponding authors

Correspondence

david.gatfield@unil.ch

david.ray@ocdem.ox.ac.uk

david.bechtold@manchester.ac.uk

Summary

Efficient energy metabolism is essential for health, and its dysregulation drives conditions like cardiometabolic disease and obesity. Delivery of regulatory control through translation and ribosome function is emerging as important. Here, we identify the rRNA methyltransferase BUD23 as a potent regulator of cellular and systemic energy homeostasis. Adipocyte-specific deletion of BUD23 in mice regulates lipid and mitochondrial metabolism resulting in a pronounced lean phenotype and resistance to diet-induced obesity. Mechanistically, BUD23 modulates translation initiation and efficiency of mRNAs with specific features – including short 5' UTR length and GC-rich post-initiation codon usage - characteristic of mitochondrial and lipogenic proteins. Human genetic analyses and drug-target Mendelian Randomisation support a role for BUD23 in cardiometabolic traits and diseases. Together, our findings uncover a conserved translational control mechanism that regulates energy metabolism and offers a potential therapeutic target.

Keywords

energy metabolism, ribosome, adipose, liver, translation, RNA methyltransferase, mTOR

Introduction

Despite recent advances in weight-loss therapies, maintaining long-term energy balance and metabolic health remains a major challenge. Fundamental questions also persist around the molecular and cellular events which set the metabolic programmes of diverse cell types across the body and how they adapt to nutrient excess or deprivation. While transcriptional regulation has been a major focus, growing evidence points to selective control over messenger RNA (mRNA) translation as a key layer of metabolic regulation [1]. Ribosomes, traditionally viewed as uniform translation machines, are now recognised to exhibit compositional and functional heterogeneity, enabling selective translation of specific mRNA subsets tailored to cell identifiy and function [2-5].

Ribosomal RNA (rRNA) plays a central role in ribosomal structure and function, ensuring proper positioning of mRNA and transfer RNA (tRNA) to facilitate accurate codon recognition, which is crucial for maintaining translation fidelity. The small ribosomal subunit (40S) is tasked with decoding the genetic information. Its decoding centre closely monitors the base pairing between the mRNA codon and the anticodon of the aminoacyl-tRNA, thus ensuring correct amino acid incorporation into the growing peptide chain. Eukaryotic rRNA harbours over 200 post-transcriptionally modified nucleotides [6] – most commonly involving methylation – many of which occur at highly conserved and functionally important sites. Recent studies suggest these modifications can be dynamic [7], raising the possiblilty that rRNA modifications are a potential driver of ribosomal heterogeneity [7]. However, the functional impact of many such modifications and their potential role in selective translational control remain unclear.

BUD23 (also known as WBSCR22/MERM1) is a highly conserved rRNA methyltransferase that has been implicated in the biogenesis and maturation of the 40S subunit and that acts together with its obligate dimerization partner, TRMT112, to modify guanosine 1639 (G1639) on human 18S rRNA to N(7)-methylguanosine (m^7G) [8-10]. This specific modification has long been recognised, but remains of unknown functional consequence to translation. Our prior work demonstrated that global *Bud23* deletion in mice results in embryonic lethality, and its

cardiomyocyte-specific deletion results in early postnatal death from cardiac failure, associated with altered mitochondrial function and insufficiency in cardiomyocyte energy production [11]. These severe phenotypes limited mechanistic exploration.

Here, we investigate the role of BUD23 in energy metabolism using tissue-specific deletion in adipocytes and hepatocytes – key metabolic cell types. We show that BUD23 is a critical regulator of lipid and mitochondrial metabolism, with distinct effects depending on cell context. Mechanistically, we uncover a BUD23-dependent program of selective translational efficiency. BUD23-sensitive transcripts share distinct 5′ mRNA features, incuding short 5′ untranslated regions (UTRs), the presence of upstream open reading frames (uORFs), and high GC content immediately downstream of the translation start codon. These features are enriched among nuclear-encoded mitochondrial genes and lipogenic regulators, explaining metabolic phenotypes of BUD23 loss. Structural modelling of 48S pre-initiation complexes further supports a role for the BUD23-catalyzed m^7G1639 modificaiton in translation initiation, via direct contacts with the initiator tRNA. Finally, human genetic analyses and Mendelian randomization indicate that BUD23 expression is associated with cardiometabolic traits including hepatic lipid content, body mass index, and obesity. Together, our findings identify BUD23-directed rRNA modification as a central regulator of selective translation and cellular energy state, with broad relevance to metabolic health and disease.

Results

Bud23 is essential for normal lipid distribution and storage in white adipose tissue.

To interrogate the role of BUD23 in regulating energy metabolism in mammals, we generated mice with selective deletion of *Bud23* in white and brown adipocytes using established transgenic lines (*Bud23*$^{fl/fl}$ [11]*; Adipoq*^{Cre} [12]; **Figure S1A,B**).

Under *ad libitum* feeding conditions with standard chow diet, growth and body weight were similar between male mice lacking *Bud23* in adipocytes (*Bud23*$^{fl/fl}$*;Adipoq*^{Cre}, designated herein as Ad^{KO}) and their littermate controls (*Bud23*$^{fl/fl}$, designated Ad^{WT}; **Figure 1A**). However, analyses of body composition revealed a striking phenotype, wherein Ad^{KO} mice exhibited a pronounced attenuation of fat mass accumulation and a significant increase in lean mass relative to controls (**Figure 1B**). This lean phenotype in Ad^{KO} mice was not associated with altered food intake (**Figure 1C**), nutrient absorption (as judged by faecal energy content; **Figure 1D**), or locomotor activity (**Figure 1E**). We did observe a small, and statistically significant, increase in daytime body temperature in the Ad^{KO} mice (**Figure S1C**). However, housing the animals at thermoneutral conditions (28°C for 6 weeks) failed to normalise genotype differences in fat mass (**Figure S1D,E**), indicating that altered thermoregulation did not underly the altered adiposity of the Ad^{KO} mice. A similar lean phenotype was observed in female Ad^{KO} animals (**Figure S1F,G**).

We next profiled metabolic gas exchange and energy expenditure. Despite the lean phenotype, Ad^{KO} mice presented lower daily energy expenditure (**Figure 1F**). Furthermore, the mice exhibited a blunted diurnal profile in respiratory exchange ratio (RER) due principally to a significant reduction in RER at night relative to control mice (**Figure 1G,H**). RER broadly reflects fuel utilisation (carbohydrate oxidation: RER ~1 vs fatty acid oxidation: RER ~0.7), and RER values >1 can indicate elevated rates of lipogenesis [13]. Our findings thus suggest that the mice lacking BUD23 activity in adipocytes exhibit increased reliance on fatty acid oxidation and, possibly, reduced rates of *de novo* lipogenesis (DNL), both of which would contribute to the reduced fat mass.

Attenuated whole body fat mass in the Ad^{KO} mice was reflected in a significant reduction in subcutaneous and visceral white adipose tissue (WAT) depots, starting at early age and greatly accentuated in older mice (**Figure 1B,I**; **Figure S1H,I**). Interestingly, histological analyses of gonadal WAT (gWAT) sections revealed relatively normal adipocyte morphology in the remaining WAT of these animals (**Figure 1I**, insets; **Figure S1J,K**). Serum triglycerides (TG) were unchanged between genotypes, yet Ad^{KO} presented with significantly lower serum levels of non-esterified fatty acids (NEFA) and glycerol, even at relatively early age (**Figure 1J)**. This suggests that reduced fat storage was not due to excessive lipolysis. To characterize adipose function more broadly, we next assessed circulating adipokine levels. In line with the lean phenotype, leptin, adiponectin, and resistin levels were all reduced in the Ad^{KO} mice (**Figure 1K**), although the magnitude of effect implicates a more direct impact to adipokine production. Together, these findings highlight the profound disturbance in WAT function of Ad^{KO} animals.

Given the significant attenuation of lipid storage in WAT, we next investigated possible compensatory accumulation of lipids within brown adipose tissue (BAT) and liver. Evident at the point of tissue dissection and further confirmed by histological examination, BAT showed accentuated lipid accumulation ("*whitening*"; **Figure 1L**) in the Ad^{KO} mice compared to controls. Similarly, the livers of these mice showed increased weight and TG content (**Figure 1M,N**). These findings suggest that attenuated WAT lipid storage capacity upon loss of BUD23 function drives excess secondary storage in organs such as liver and BAT. Stable isotope labelling with $^{2}H_2O$ (in drinking water, 48 hr) and [^{13}C]-labelled D-glucose (bolus administration following short-term fasting) was used to assess rates of DNL across these tissues. Higher rates of hepatic DNL were confirmed by increased incorporation of both labels into palmitic acid (16:0) in the Ad^{KO} mice relative to controls (**Figure 1O,P**). By contrast, no differences were observed in BAT (**Figure 1O,P**), although local alteration in rates of DNL may be masked by uptake of lipids from the liver. The observed increase in size, TG content, and DNL in the liver underscores a shift in lipid metabolism and storage dynamics in response to adipocyte-specific *Bud23* deletion.

In the Ad^{KO} model, the deletion of *Bud23* occurs in both white and brown adipocytes. However, the phenotypic outcomes described above revealed striking differences, with attenuated and accentuated lipid accumulation in WAT and BAT, respectively. We hypothesised that the whitening of BAT in the Ad^{KO} mice may be secondary to defective lipid storage in WAT. To address this possibility, we generated a *Bud23*$^{fl/fl}$;*Ucp1*^{Cre} mouse line (BAT^{KO}), in which *Bud23* is selectively deleted from only brown adipocytes. No differences in body weight, adiposity, or WAT depot weight were apparent in the mice (**Figure S2A-D**). However, intrascapular BAT tissue was significantly smaller and showed no evidence of whitening in the BAT^{KO} mice compared with littermate controls (**Figure S2E**). The animals showed no overt differences in metabolic or thermogenic phenotype (**Figure S2F-G**). These analyses highlight that while loss of *Bud23* clearly impacts BAT, the accentuated lipid accumulation in this tissue observed in the Ad^{KO} mice is secondary to WAT dysfunction.

In an attempt to drive lipid accumulation in adipose tissues, we placed Ad^{WT} and Ad^{KO} mice onto high-fat diet (HFD; 60% energy from fat). As expected, control mice gained significant body weight and fat mass over the 9-week HFD treatment (**Figure 1Q-S**). In contrast, Ad^{KO} mice were highly resistant to diet-induced obesity, accumulating significantly less fat mass. These findings demonstrate that adipocyte-specific *Bud23* deficiency impairs WAT lipid storage irrespective of whether the dietary energy source is carbohydrate-rich or fat-rich.

In summary, our results demonstrate that BUD23 is essential for lipid accumulation in WAT. The absence of complete adipocyte loss implies that explanations, such as defects in cell differentiation or survival, are unlikely to account for the observations. Instead, BUD23 appears to play a role in maintaining long-term lipid storage in WAT and preservation of mature white adipocyte function.

Bud23 is required for white adipocyte function, but not differentiation

We next isolated stromal vascular fraction (SVF) cells from gWAT of Ad^{KO} and Ad^{WT} mice to directly examine adipocyte differentiation capacity *in vitro*. No defects in adipocyte differentiation efficiency, lipid accumulation, or lipid droplet formation in cells derived from Ad^{KO} animals were observed (**Figure S3A,B**). Furthermore, within these newly differentiated adipocytes, expression levels of endocrine hormones and lipid metabolism enzymes were normal (**Figure S3C**). Hence, the lean phenotype observed in Ad^{KO} mice *in vivo* is not due to an impaired capacity of adipocytes to differentiate.

Transcriptomics analyses on gWAT isolated from ~13-week old Ad^{KO} and Ad^{WT} mice (thus prior to the profound differences in fat mass that develop with age) revealed widespread differential gene expression associated with *Bud23* deletion (**Figure 2A**). We first assessed whether tissue cellular composition contributed to the transcriptional signatures observed. We therefore performed virtual cytometry analyses using CIBERSORT deconvolution [14], and leveraging published single-cell RNA-seq data from mouse gWAT [15] (**Figure 2B**). While these analyses did not reveal profound changes to cell type composition, including adipocyte precursors, notable exceptions emerged. This included a significant reduction in *lipid scavenging adipocyte* (LSA) and *lipogenic adipocyte* (LGA) subpopulations, and a strong increase in *stressed lipid scavenging adipocytes* (SLSA) (**Figure 2B,C**). Although these analyses only infer cellular composition, the results align well with the observed *in vivo* phenotype. LGAs, which are characterised by high expression of genes involved in lipid biosynthesis and insulin responsiveness, likely contribute to DNL and efficient lipid storage [15]. Their depletion in Ad^{KO} mice, coupled with the concomitant increase in SLSAs, suggests a failure to properly manage and store lipids in the absence of BUD23.

We next undertook pathway enrichment on the gWAT transcriptomics. Ingenuity Pathway Analysis (IPA) revealed a striking downregulation of mitochondrial pathways, broadly affecting key metabolic processes, including respiratory electron transport, ATP synthesis, fatty acid β-oxidation, and branched-chain amino acid degradation (**Figure 2D**; **Figure S3D**). Increased mitochondrial dysfunction was also predicted. Examination of key differentially expressed genes involved in adipocyte function, lipid metabolism, and mitochondrial activity revealed their extensive downregulation in Ad^{KO} (**Figure 2E**). The reduced expression of adipokine genes, such as *Leptin (Lep)*, *Adiponectin (Adipoq)* and *Resistin (Retn)*, was also consistent with the observed endocrine profiles of Ad^{KO} mice (**Figure 1K**). Importantly, *Bud23* deletion did not cause uniform repression of all adipocyte-specific or metabolic genes. Instead, selective impact to key metabolic pathways, such as fatty acid synthesis, was evident. For example, *Fatty acid synthase* (FAS), key enzyme in fatty acid synthesis, exhibited a striking decrease in protein abundance in Ad^{KO} WAT, while other markers remained relatively unchanged (**Figure 2F**). Analysis of mature adipocytes isolated directly from gWAT of Ad^{KO} and Ad^{WT} mice confirmed that observations made in whole tissue RNA-seq reflected *Bud23*-dependent reprogramming of white adipocytes *per se* (**Figure 2G**).

Given the well-established influence of insulin over adipocyte function, we assessed insulin sensitivity in Ad^{KO} and Ad^{WT} mice. *In vivo*, clearance of circulating glucose in response to acute insulin administration was significantly attenuated in the knockout mice when compared to controls (**Figure 2H**). *In vitro*, gWAT explants derived from Ad^{KO} mice showed a profoundly attenuated induction of *Dgat2*, *Fasn*, and *Fabp4* following insulin treatment, compared to the response in Ad^{WT} explants (**Figure 2I**).

We concluded from the above experiments that *Bud23* exerts profound influence over white adipocyte function, yet its effects are selective, with mitochondrial metabolism and lipid biosynthesis as key targets.

BUD23 influence over lipid metabolism and mitochondrial function is conserved across white and brown adipose

White and brown adipocytes diverge in functional specialisation, with white adipocytes central to storage and liberation of energy (principally as TG/FAs) based on changing energy demands, while brown adipocytes oxidise FAs almost exclusively for the generation of heat. Therefore, we next assessed BAT function in the Ad^{KO} mice to identify shared and divergent roles of BUD23 between these two adipose depots.

As highlighted above (**Figure S1D**), Ad^{KO} mice exhibited relatively normal profiles in body temperature suggesting maintained BAT function. This was confirmed through direct assessment of interscapular BAT temperature under normal housing conditions (~22°C±2°C; **Figure 3A,B**). Moreover, both genotypes robustly maintained body temperature throughout the cold challenge (**Figure 3C,D**). In line with robust thermogenic capacity, BAT *Ucp1* did not differ between the genotypes at the level of RNA or protein expression (**Figure S4B,D**); although significant differences were observed in other thermogenesis-related transcripts. We therefore undertook RNA-seq analyses on BAT tissues derived from Ad^{KO} and control mice, which identified significant numbers of differentially expressed RNAs (**Figure 3E**). IPA pathways analyses of the RNA-seq data revealed clear enrichment of mitochondrial protein-encoding transcripts – characterized by the downregulation of key metabolic pathways such as fatty acid oxidation, the tricarboxylic acid (TCA) cycle, the respiratory chain, and branched-chain amino acid catabolism (**Figure 3F**).

Given that BUD23 is an enzyme known to modify rRNA near the ribosomal decoding centre [9], altered translation is a likely consequence of *Bud23* deletion. Indeed, proteomic analyses of identified widespread differential protein expression between Ad^{KO} and Ad^{WT}-derived BAT (**Figure 3G**). IPA pathway analyses revealed a significant enrichment for mitochondrial proteins and those involved in branched chain amino acid (BCAA) metabolism (**Figure 3H**). Downregulation of BCAA upon loss of *Bud23* has been consistently observed between WAT and BAT analyses, with pronounced reduction in the expression of key enzymes such as BCAT2 observed (**Figure S4E**). Interestingly, the proteomics analysis of BAT also identified two ribosome/translation-associated pathways as significantly dysregulated: the *Regulation of eIF4 and p70S6K Signalling* and *mTOR Signalling* pathways. Both pathways involve overlapping gene sets that include ribosomal protein genes, translation initiation factors, and key signalling components critical for regulating both global and transcript-specific translation in response to hormones, nutrients, stress, and other signals. These findings were similarly reflected in ontology analyses which highlighted the significant down-regulation of proteins

involved in mitochondrial function, lipid metabolism and ribosomal subunit biogenesis (**Figure S4D**).

Assessment of genotype-specific differences in global protein abundance revealed a particular impact on expression of small subunit ribosomal proteins (RPS) and mitochondrial proteins (based on MitoCarta3.0; **Figure 3I**). RPS protein changes were expected given the known role of BUD23 in small ribosomal subunit maturation [8,16,17], yet the clear impact of *Bud23* loss on mitochondrial genes and proteins prompted us to assess BAT mitochondrial content. This revealed a significant reduction in mitochondrial DNA copy number (**Figure 3J**) and reduced mitochondrial area assessed using electron microscopy (EM; **Figure 3K,L**) in *Bud23*-deficient BAT.

Thus, across both WAT and BAT, BUD23 function has relatively select influence over mitochondrial factors and lipid metabolism. Recent evidence highlights an important role for mitochondrial dynamics and its physical interaction with the endoplasmic reticulum (ER) and lipid droplets (LD) in regulating cellular energy metabolism [18,19 20]. Intriguingly, proteins which were significantly down-regulated in BAT of Ad^{KO} mice included several factors which dictate these inter-organelle interactions (e.g. MFN1/2, OPA1, MIGA2), and up-regulation in LD coat proteins (e.g. PLIN2, PLIN5).

Together, our results demonstrate that the loss of *Bud23* from adipocytes drives pronounced impact to mitochondrial, lipogenic, and ribosomal protein expression. Given BUD23's role in 18S rRNA modification, the observed phenotypes likely stem from altered translational dynamics as a primary mechanism. Our proteomic data are consistent with this model, revealing coordinated shifts in protein abundance consistent with disrupted translation. However, widespread transcriptional changes and the broad metabolic disruption observed upon *Bud23* deletion likely inlcude both primary and secondary effects, limiting resolution of direct versus indirect targets in the adipose tissue models.

Hepatic targeting of *Bud23* reveals selective impact to energy homeostasis and mitochondrial metabolism

Due to its relatively homogenous cellular composition, large size, and high metabolic activity, we considered the liver well-suited for investigating the functional impact of BUD23 on translation. To this end, we generated a hepatocyte-specific *Bud23* deletion by crossing $Bud23^{fl/fl}$ mice with the well-established inducible $Alb^{CreERT2}$ line [21]. Tamoxifen administration to $Bud23^{fl/fl}$;$Alb^{CreERT2}$ (Liv^{KO}) and control $Bud23^{fl/fl}$ (Liv^{WT}) animals resulted in a robust reduction in *Bud23* expression in Liv^{KO} animals (**Figure S5A,B**).

We first profiled the Liv^{KO} model for overt metabolic phenotypes. Under standard conditions, no significant differences between Liv^{KO} and Liv^{WT} mice were observed for body weight, body composition, energy expenditure, RER, or food intake (**Figure 4A-F**). Interestingly, despite this overall metabolic similarity, hepatic TG levels were elevated in LivKO mice (Figure 4G). Notably, in response to metabolic challenges driving either positive or negative energy balance (HFD-feeding and fasting, respectively), *Bud23*-dependent phenotypes emerged. Firstly, during 8 weeks of HFD feeding, Liv^{KO} and Liv^{WT} mice showed similar profiles of body weight gain (**Figure 4G**), yet hepatic TG levels were still elevated in Liv^{KO} (**Figure 4H**). Secondly, when subject to an extended fast (48 h), Liv^{KO} mice exhibited significantly attenuated β-hydroxybutyrate production, despite showing similar levels of body weight loss and

hypoglycaemia (**Figure 4K-L**). Both findings are consistent with altered mitochondrial activity (e.g. β-oxidation, BCAA) and lipid handling.

Given our findings in WAT and BAT, we examined the impact of *Bud23* loss on mitochondrial content, structure and function in the livers of Liv^{KO} and Liv^{WT} mice. Firstly, overall mitochondrial copy number was unchanged (**Figure S5C**). However, EM analyses revealed a slight reduction in mitochondrial area in Liv^{KO}, although this difference did not reach statistical significant (**Figure 4M,N**). Given that mitochondrial morphology is associated with changes in function [22,23], we next assessed isolated hepatic mitochondrial respiration using the OROBOROS platform (**Figure 4O-Q**). Respiration rates measured in isolated mitochondria in the presence of complex I substrates and saturating levels of ADP (State III respiration; OXPHOS) were comparable between genotypes. However, a significant elevation in State IV respiration (LEAK) reflecting proton leak-driven respiration was evident in the mitochondria isolated from Liv^{KO} mice. This in turn resulted in a significantly reduced respiratory control ratio (RCR), strongly suggesting that mitochondrial ATP production will be less efficient in Liv^{KO} tissue, driven by an increase in proton leak.

Collectively, our findings demonstrate that mitochondrial dysfunction and lipid metabolism alterations are common features of *Bud23* deficiency across tissues.

Hepatic *Bud23* loss drives selective impact on translation

We next interrogated the molecular mechanism of BUD23 action in the liver. To assess its impact on translation, we quantified mRNA abundances and ribosome occupancy using RNA-seq and ribo-seq, respectively, in liver tissue from Liv^{KO} and Liv^{WT} animals. To capture early effects in translational reprogramming while minimizing secondary effects, we used a relatively early timepoint (3 weeks post-tamoxifen induction), and given the well-documented rhythmicity of hepatic metabolic activity, gene expression, and translation [24], we collected samples at two times of day corresponding to fasted (*Zeitgeber* Time ZT6; mid-light phase) and fed (ZT18; mid-dark phase) states (**Figure S6A)**. Principal component analyses (PCA) revealed clear separation based on genotype (Liv^{KO} vs Liv^{WT}; PC1), followed by time-of-day (ZT6 vs ZT18; PC2) for the RNA-seq (**Figure S6B)** and ribo-seq (**Figure S6C**) datasets. In contrast, the PCA for translation efficiencies (TEs; ratio of ribo-seq to RNA-seq counts) indicated a strong genotype effect, with less influence of time (**Figure S6D**). Therefore, unless otherwise noted, subsequent analyses were performed using combined timepoint data.

RNA-seq and ribo-seq analyses revealed widespread *Bud23*-dependent differential gene expression and ribosome occupancy (**Figure 5A,B**). A subset of genes exhibited altered ribosome engagement, and thus significant change in TE (decreased TE: n=105; increased TE: n=179; **Figure 5C**). GO term analyses of each dataset identified key functional transcript groups (**Figure 5D**). Notably, genes encoding ribosomal proteins (RPs) and other ribosome-related factors were associated with increased transcript abundance and TE, possibly reflecting a compensatory response to inactivation of BUD23. In contrast, downregulated transcripts were enriched for metabolic and mitochondrial functions. These metabolic GO terms did not reach statistical significance for the differential TE cluster, although several individual genes of note did emerge including *Agpat2, Agpat3, Sirt3, RXRa*.

We further examined translational changes across all nuclear-encoded genes specifying mitochondrial proteins (from MitoCarta 3.0 [25]). RNA-seq (**Figure 5E**), ribo-seq (**Figure 5F**), and TE (**Figure 5G**) all revealed significant downregulation in Liv^{KO} samples for this

mitochondrial gene set, whereas ribosome-related transcripts showed strong upregulation, particularly evident in TE. Many mRNAs encoding RPs and translation factors contain 5'-terminal oligopyrimidine (TOP) motifs, which are key targets of mTOR-mediated translation regulation, allowing cells to adapt protein synthesis to metabolic/environmental changes [26]. Under normal conditions, RP mRNAs are highly abundant and exhibit rhythmic translation, with lower translation rates during the fasting (light) phase and upregulated translation upon feeding in the dark phase [24,27,28]. We found *Bud23* deficiency to affect strongly this regulation; thus, in Liv^{WT} tissue, the TEs for a set of 5'-TOP mRNAs showed significant time-of-day dependent increase (from ZT6 to ZT18), consistent with mTOR-driven translational control associated with feeding state (**Figure 5H**). In Liv^{KO} samples, TEs were strikingly elevated across both timepoints and the rhythmic patterns was strongly blunted. This suggests that BUD23 function is required for normal translational regulation of 5'-TOP mRNAs.

For TE calculations, ribosome footprint reads are counted over the entire CDS, without considering local variations in ribosome occupancy. However, changes in ribosome dwelling can provide deeper insights into translation regulation and kinetics. To assess whether BUD23 influences specific decoding events, we applied a pipeline to infer elongation dynamics based on transcriptome-wide codon occupancies associated with the ribosomal E-, P-, and A-sites [29]. This analysis confirmed known differences in decoding speeds across codons in both Liv^{KO} and Liv^{WT} samples, but revealed only minor genotype-associated changes (**Figure S6E,F**), suggesting that overall translation elongation dynamics remain largely robust. A metagene approach was next used to visualize transcriptome-wide ribosome footprint distributions along the 5′ UTR, CDS, and 3′ UTR. This analysis revealed two striking differences between genotypes (**Figure 5I**). First, in Liv^{WT}, we observed the expected low, but readily detectable footprint coverage on 5′ UTRs, consistent with pervasive upstream open reading frame (uORF) translation and as seen in previous liver ribo-seq datasets [24]. In contrast, Liv^{KO} samples showed a significant depletion of 5′ UTR-mapping reads (**Figure 5I,J**). Second, the Liv^{WT} metagene plot displayed the characteristic "translational ramp" – a region of elevated ribosome density at the beginning of the CDS, which gradually declines as elongation progresses (**Figure 5I**). This ramp was largely absent in Liv^{KO} samples (**Figure 5I**, inset), with significantly reduced ribosome occupancy within the first 20 codons post-initiation (**Figure 5J**). The reduced 5′ UTR occupancy and loss of the ramp in Liv^{KO} suggests a disruption in early ribosome dynamics, reinforcing the idea that BUD23 influences translation initiation rather than elongation.

To understand how BUD23 activity may impact initiation, we examined available ribosomal structures from cryo-electron microscopy datasets capturing key intermediates of the human initiation pathway [30]. In these structures, m^7G1639 is located in immediate vicinity to the P-site-bound initiator-tRNA (Met-$tRNA_i^{Met}$), interacting with C41 of its anticodon stem loop via hydrogen bonding (**Figure 5K, S7**). The C41 residue is critical for maintaining the unique conformation of initiator-tRNA, distinguishing it from elongator tRNAs, and ensuring proper start codon recognition [31]. Our structural analyses indicate that the N7-methyl group of m^7G1639 fills a hydrophobic pocket that helps stabilize this interaction, while the positive charge conferred onto the guanosine ring by the methyl group (quaternary nitrogen at N7) enables cation-π stacking with Trp35 of ribosomal protein sE25/RPS25, particularly in the late initiation complex 48S-5 (**Figure 5K**). This interaction likely further secures G1639 in an optimal orientation for initiator-tRNA placement. In the absence of m^7G1639 methylation (as in *Bud23* knockouts), it is likely that weakened interaction at this site would alter the precision and stability of initiator-tRNA engagement at the start codon.

In summary, we concluded that loss of BUD23 function leads to a selective changes to translation, particularly impacting mRNA encoding ribosomal proteins and mitochondrial components. Mechanistically, the association of BUD23 loss with lower 5′ UTR occupancy and loss of a translational ramp, as well as structural considerations, suggest predominant effects on initiation.

GC content, 5′ UTR length and uORF content predict mRNA responsiveness to BUD23 and are associated with selective effects on mitochondrial transcripts

We next examined whether changes in CDS TE, reduced ribosome occupancy over the first 60 nt after translation initiation (i.e., absence of ramp; hereafter referred to as 'Start TE'), and decreased 5′ UTR coverage ("outcomes" in **Figure 6A**, upper) were associated with specific transcript features that predict mRNA responsiveness to BUD23 activity ("features" in **Figure 6A**, lower). Correlation analyses indicated that genotype-related fold changes (FCs) in 5′ UTR coverage, Start TE (corrected for CDS TE effects), and CDS TE were largely independent (**Figure S8A-E**), allowing them to be handled as individual outcomes.

We assessed several transcript characteristics potentially associated with these outcomes (**Figure 6A**, lower). Specifically, 5′ UTR-related features included the presence of uORFs (initiated by ATG or C/G/T TG); 5′ UTR length (based on mouse liver CAGE data); and 5′ UTR GC content. In the CDS start codon environment, we quantified the Kozak sequence score; three proxies for RNA structure – GC-content in a 60 nt window preceding the initiation codon (-60 nt) or following it (+60 nt, ramp region), and RNA folding minimal free energy (MFE) over the ±60 nt window; as well as codon bias (low scores indicate higher proportion of rare codons).

Transcriptome-wide analyses showed that lower 5′ UTR coverage in Liv^{KO} was primarily correlated with 5′ UTR length and the presence of translated uORFs, and anticorrelated with 5′ UTR GC content (**Figure 6B, S8F,G**). For CDS TE and normalised Start TE we detected strong anticorrelation with GC content (in the 5′ UTR and around the initiation codon), as well as with MFE. Kozak score (i.e., CDS initiation codon optimality) and bias in codon composition showed no, or only weak, correlations. As expected, several of the analysed features are intrinsically correlated with each other – for example, UTR length and uORF frequency, or GC content in the 5′ UTR and around the initiation codon (**Figure S8H**). To disentangle these effects, we applied linear regression modelling to identify the primary predictors of variance in the translation outcomes. The model identified 5′ UTR GC content as the predominant predictive feature throughout (**Figure S8I**) with variable additional contributions from 5' UTR length/CAGE distance, RNA folding MFE, and other predictors to lesser extent.

We observed globally lower CDS TE for mitochondrial protein mRNAs in Liv^{KO} liver tissue (**Figure 5G**). Moreover, the metagene plot on mitochondrial transcripts also revealed particularly marked footprint reduction directly downstream of the CDS start codon (**Figure 6C**). We therefore examined if these effects on mitochondrial mRNAs were associated with any of the above transcript features. In these analyses (**Figures 6D-F, S8J-O**), we observed that the GC content in the 60 nt downstream of the start codon (**Figure 6D**) was specifically elevated among mitochondrial transcripts. This effect was accompanied by increased RNA folding MFE (**Figure S8L**) and pronounced codon bias in the first 60 nt of mitochondrial protein CDS (**Figure 6E**). Metagene analyses on transcript sets selected for high vs. low +60 GC contents further revealed the profound influence that GC content after the start codon has over

ribosomal occupancies post-initiation (**Figure S8P**). For mitochondrial transcripts, GC-content is indeed specifically increased in the post-initiation region (**Figure S8Q**), where codon composition is biased towards GC-rich codons for alanine, arginine and leucine (**Figure 6G**). These are common amino acids in the amphipathic α-helices that make up mitochondrial targeting signals [32]. Furthermore, the association between high +60 GC content with reduced ribosome occupancy post-initiation seen across hundreds of mitochondrial protein transcripts (**Figure 6H**) extended to the translation level of the CDS as a whole – mitochondrial transcripts scoring very high for +60 GC content thus also showed particularly reduced CDS TEs (**Figure 6I**).

Another striking mitochondrial transcript feature was short 5′ UTRs – an effect that was highly significant (**Figure 6F**) and correlated with diminished 5′ UTR ribosome occupancy in Liv^{KO} (**Figure 6J**). When we further correlated 5′ UTR length with TE changes occurring on the CDS, we observed that many mitochondrial transcripts that carried extremely short UTRs (**Figure 6J**) showed specifically strong reduction in CDS translation in Liv^{KO} tissue (**Figure 6K**). Transcripts with very short 5′ UTRs (<30 nt) are thought to be unable to assemble the translation initiation machinery via the conventional pathway and rely on specialised, poorly understood mechanisms to thread the mRNA into the 40S subunit to engage on 5′ cap-proximal start codons [33]. Our data would suggest that BUD23 is important for efficient translation of such transcripts, and the enrichment of mitochondrial transcripts among mRNAs with very short 5′ UTRs likely further contributes to their preferential deregulation in Liv^{KO} mice.

With the identification of initiation as a BUD23-responsive mechanism, and three likely correlates of transcript selectivity – GC content at the initiation codon, 5′ UTR length and uORF content – we next selected prototypic mRNAs to examine footprint distributions along the transcripts. For example, *Bola3* – encoding an essential mitochondrial [Fe-S] cluster delivery factor genetically linked to multiple mitochondrial dysfunctions syndrome (MMDS) [34] – has among the highest +60 GC contents (82%; **Figure 6H**) and shortest 5′ UTRs (<25 nt; **Figure 6K**), and it exhibited an almost 4-fold reduction in translation efficiency on the CDS (**Figure 6L**); the read distribution along the mRNA confirmed the dramatic loss in ribosome occupancy post-initiation, as well as low coverage over the remainder of the CDS (**Figure 6M**). Other mitochondrial transcripts where short 5′ UTR and high +60 GC content synergised (**Figure 6I,K**) and CDS TE was reduced (**Figure 6L**), were, for example, *Cox6a1* (a nuclear-encoded subunit of the terminal enzyme of the respiratory chain, Cytochrome c oxidase, COX) (**Figure 6N**) or *Ak3* (an adenylate kinase necessary for TCA cycle activity [35]) (**Figure 6O**). In other cases, short 5′ UTR was not associated with elevated GC content – e.g. *Uqcc2* (required for mitochondrial respiratory chain complex III assembly, [36]) (**Figure 6P**), which showed very strongly reduced translation efficiency in Liv^{KO} (**Figure 6L**). We also examined examples for genes with strong Liv^{KO}-specific reduction in ribosome occupancy on the 5′ UTR (**Figure 6R-T**). We found evidence that this was indeed frequently due to low ribosome occupancy on uORFs, as shown for the cases of *Cisd3* [37], *Etfdh* [38], and *Igfbp4*. Notably, all the implicated uORFs were localised very close to the mRNAs' 5′ cap (**Figure 6R-T**).

Taken together, the above analyses established that GC content in the early coding region, 5′ UTR length, and uORF content are key determinants of BUD23-dependent translational control of initiation. These features not only predict mRNA responsiveness but also explain the preferential impact of BUD23 loss on mitochondrial transcripts, whose structural characteristics render them particularly reliant on efficient initiation mechanisms.

BUD23 Expression is linked to human cardiometabolic and systemic traits

Given the metabolic and mitochondrial phenotype observed in *Bud23*-knockout mouse models, we sought to examine whether genetically predicted BUD23 expression in humans is associated with cardiometabolic diseases and related biomarkers. To do this, we applied drug-target Mendelian randomization (MR), a method that uses germline genetic variants as instrumental variables to estimate the causal effect of modulating gene expression on disease risk [39,40]. Specifically, we modeled BUD23 expression in whole blood using cis-eQTL variants within the BUD23 locus and assessed its effects on major cardiometabolic outcomes, including coronary artery disease (CAD), obesity, metabolic-associated steatotic liver disease (MASLD), cirrhosis, and circulating biomarkers of lipid, glucose, and liver function.

Genetically increased *BUD23* expression in whole blood was found to be inversely associated with coronary artery disease (CAD), metabolic-associated steatotic liver disease (MASLD), and liver enzymes, including alanine aminotransferase (ALT) and aspartate aminotransferase (AST), suggesting a protective effect (**Figure 7A**). We additionally observed significant inverse associations with hypertension, aligning with lower systolic blood pressure (SBP) levels, as well as a reduction in myocardial infarction (MI) risk. By contrast, increased *BUD23* expression was positively associated with body mass index (BMI) and obesity, indicating a potential trade-off between adiposity and cardiometabolic protection. Notably, effect estimates were concordant across both primary and replication GWAS sources, indicating robustness to population-specific biases and strengthening confidence in the inferred causal effects.

We next explored whether the genetic impact of *BUD23* is tissue-dependent by repeating the MR analyses using eQTLs for *BUD23* expression in adipose (subcutaneous and visceral), skeletal muscle, heart (atrial appendage), and liver (**Figure S9C**). The direction and magnitude of effects in adipose tissues closely mirrored those in whole blood, particularly for obesity, lipids, and MASLD, suggesting shared metabolic pathways. In contrast, muscle-derived *BUD23* instruments yielded directionally opposite effects, particularly for BMI and T2D. This divergence may reflect tissue-specific roles of BUD23, where increased BUD23 in muscle could alter translation of mitochondrial factors, with down-stream impact to energy efficiency.

To move beyond cardiometabolic phenotypes and capture the broader impact of *BUD23* on human health, we performed a phenome-wide MR scan across ~1,200 outcomes from the Million Veteran Program (MVP) among participants of European ancestry [41]. This analysis revealed significant enrichment of genetically proxied BUD23 expression in traits related to metabolic, hepatic, and cardiovascular function, including liver fat, dyslipidemia, hypertension, and inflammatory biomarkers (**Figure 7B**). To contextualize these findings anatomically, we visualized the top FDR-significant outcomes (FDR<0.05 per disease category) across disease domains using a homunculus-style plot (**Figure 7C**). The most prominent effects were observed in endocrine/metabolic, hepatic, and cardiopulmonary systems, reinforcing the hypothesis that BUD23 is a key regulator of systemic energy homeostasis.

Together, these findings integrate human genetic evidence with *in vivo* functional data, supporting a role for BUD23 in metabolic regulation and suggesting its potential relevance to cardiometabolic health and disease.

Discussion

BUD23 is a highly conserved 18S ribosomal RNA methyltransferase that catalyzes the formation of N^7-methylguanosine (m^7G) at position G1639 within the small ribosomal subunit and contributes to 40S subunit maturation (White et al. 2008). This modification is located near the decoding centre, adjacent to the P- (peptidyl) and E- (exit) sites, and is unique in that it introduces a positive charge and alters local steric constraints within a structurally restricted region. These local changes likely perturb ribosome-mRNA interactions in a manner that selectively alters translation dynamics. However, the physiological role of BUD23, particularly in mammalian tissues, has remained largely unexplored.

In this study, we show that BUD23 exerts selective translational control critical for mitochondrial function and lipid metabolism, with profound effects in white and brown adipose tissue as well as liver. In WAT, *Bud23* deletion causes striking mitochondrial dysfunction and loss of lipid droplet formation *in vivo*, despite relatively preserved adipocyte differentiation *in vitro*. In contrast, in BAT, loss of *Bud23* results in lipid accumulation and tissue whitening, likely reflecting impaired mitochondrial beta-oxidation. BAT is rich in mitochondria and relies heavily on mitochondrial respiration to fuel its thermogenic function (Cannon,Nedergaard, 2004). In our model, however, thermogenic function remains largely preserved, pointing to a distinct and intriguing mitochondrial phenotype. In summary, the opposing adipocyte phenotypes – lipid loss in WAT and lipid accumulation in BAT – underscore a shared mitochondrial dysfunction but reveal tissue-specific consequences, potentially driven by differences in mitochondrial content and the energy storage vs. expenditure roles of these adipose depots.

The liver exhibits a milder phenotype, but mitochondrial defects remain a primary outcome. This is supported by our ribosome profiling data that revealed changes to the translation of mRNAs specifying nuclear-encoded mitochondrial proteins. Mechanistically, our findings support a model in which BUD23-modified ribosomes are optimized for translation of a critical subset of mitochondrial mRNAs. These transcripts often bear structural and sequence features that can challenge canonical initiation, such as very short 5′ UTRs and high GC content immediately downstream of the initiation codon. This GC bias is a predictable consequence of the amino acid composition of N-terminal mitochondrial targeting sequences, which are often amphipathic and rich in arginine and leucine. These features may predispose such transcripts to inefficient initiation, making them particularly dependent on BUD23-modified ribosomes for effective translation. This model provides a mechanistic explanation for the coherent mitochondrial dysfunction across tissues.

We also uncover a disruption in energy-sensitive translational regulation. Normally, 5′ TOP-containing mRNAs – mostly encoding ribosomal proteins and translation factors – respond dynamically to nutrient availability via mTOR signalling. In *Bud23*-deficient livers, this regulation is abrogated: 5′ TOP mRNA translation remains elevated during the light/fasting phase, indicating a decoupling of nutrient sensing and translational control. This may reflect altered ribosome activity due to altered 40S maturation or mRNA engagement during initiation, suggesting that *Bud23* contributes to the broader translational architecture that enables metabolic adaptation. While the precise integration of global and transcript-selective effects remains unclear, the observed specificity for mitochondrial mRNAs is not readily explained by general effects in ribosome biogenesis alone. These findings argue for an active regulatory role for BUD23's methyltransferase activity in shaping the translational landscape.

An intriguing possibility raised by our findings is that m^7G1639 modification may not be constitutive but instead dynamically regulated. Although BUD23 is generally considered a

constitutive factor, growing evidence from other rRNA-modifying enzymes suggests that activity and expression may vary across tissues and physiological states. Indeed, viral manipulation of the BUD23-dependent methylation site has recently been described [42], raising the possibility of endogenous regulation. If so, dynamic installation of this rRNA modification could provide a powerful mechanism to tune ribosome activity and selectively modulate translation of metabolically critical transcripts. This raises the exciting possibility that BUD23 itself may be modulated by metabolic inputs, forming a feedback loop between nutrient state, translational output, and energy homeostasis. Moreover, a broader rRNA-modification network – including other TRMT112 partners such as METTL5 [43] – may have evolved to tune ribosomal activity according to metabolic needs.

Finally, our study connects these mechanistic insights to human health. While BUD23 has previously been associated with cancer and inflammatory disease [44-46], its role in metabolic organs had not been clearly defined beyond our previous work [11]. Notably, BUD23 is located within the critical deletion region of Williams-Beuren Syndrome (WBS), a multisystem disorder characterized by cardiovascular and metabolic phenotypes [47]. Although multiple genes are deleted in WBS, our finding that *BUD23* is strongly associated with liver fat content (MASLD), body mass index, and obesity suggests it may meaningfully contribute to the metabolic features of this syndrome. Extending our large-scale genetic analysis to the related *METTL5* revealed partially overlapping protective associations, whereas TRMT112 showed minimal effects. These findings integrate functional and genetic data to support a key role for BUD23 in metabolic homeostasis and underscore its potential relevance to cardiometabolic health and disease.

Together, our findings define BUD23 as a key regulator of ribosome specialization, selectively enhancing translation of mitochondrial mRNAs critical for energy metabolism. By linking nutrient sensing, translational control, and mitochondrial function, BUD23 emerges as a central node in the regulation of metabolic homeostasis.

Acknowledgment

We thank and acknowledge support of core facilities at the University of Manchester: Bioinformatics Core Facility, UoM Genomic Technologies Core Facility, Biological Services Unit, and Histological Services Unit, and at the University of Oxford: Dr. Anne Clark and the Electron Facility (Dunn School) for their advice on Electron Microscopy imaging, Amy Barret for her support with biochemistry analysis, and The Target Discovery Institute Mass Spectrometry group for the support on proteomic analysis. We thank Dr. Ana Domingos for thermal imaging equipment use. D.G. acknowledges funding by the University of Lausanne and by the Swiss National Science Foundation (SNSF, grants 212423, 10002692, and NCCR RNA & Disease, 205601). D.A.B acknowledges funding by the Medical Research Council (MRC) (MR/P00279X/1). D.W.R acknowledges funding by NIHR Oxford Health Biomedical Research Centre (NIHR203316) and MRC (MR/W019000/1 and MR/V034049/1).

Author contributions

Conception: D.B., D.R., and D.G. Methodology: N.M-S, A.B., N.J.B., D.B.R, A.L, M.V., E.A.H., S.C., R.D., N.G., E.J., M.B., K.S., R.C.N., G.G., L.H. Original draft: N. M-S, D.B., D.R., and D.G. Revisions: N. M-S, A.B., L.H., D.B., D.R., and D.G. Supervision: D.B., D.R., and D.G.

Declaration of interests

The authors declare no competing interests.

References

1. Shu, X.E., Swanda, R.V., and Qian, S.B. (2020). Nutrient Control of mRNA Translation. Annu Rev Nutr *40*, 51-75. 10.1146/annurev-nutr-120919-041411.
2. Kondrashov, N., Pusic, A., Stumpf, C.R., Shimizu, K., Hsieh, A.C., Ishijima, J., Shiroishi, T., and Barna, M. (2011). Ribosome-mediated specificity in Hox mRNA translation and vertebrate tissue patterning. Cell *145*, 383-397. 10.1016/j.cell.2011.03.028.
3. Ferretti, M.B., Ghalei, H., Ward, E.A., Potts, E.L., and Karbstein, K. (2017). Rps26 directs mRNA-specific translation by recognition of Kozak sequence elements. Nat Struct Mol Biol *24*, 700-707. 10.1038/nsmb.3442.
4. Hebras, J., Marty, V., Personnaz, J., Mercier, P., Krogh, N., Nielsen, H., Aguirrebengoa, M., Seitz, H., Pradere, J.P., Guiard, B.P., and Cavaille, J. (2020). Reassessment of the involvement of Snord115 in the serotonin 2c receptor pathway in a genetically relevant mouse model. eLife *9*. 10.7554/eLife.60862.
5. Jansson, M.D., Häfner, S.J., Altinel, K., Tehler, D., Krogh, N., Jakobsen, E., Andersen, J.V., Andersen, K.L., Schoof, E.M., Ménard, P., et al. (2021). Regulation of translation by site-specific ribosomal RNA methylation. Nat Struct Mol Biol *28*, 889-899. 10.1038/s41594-021-00669-4.
6. Taoka, M., Nobe, Y., Yamaki, Y., Sato, K., Ishikawa, H., Izumikawa, K., Yamauchi, Y., Hirota, K., Nakayama, H., Takahashi, N., and Isobe, T. (2018). Landscape of the complete RNA chemical modifications in the human 80S ribosome. Nucleic Acids Res *46*, 9289-9298. 10.1093/nar/gky811.
7. Milenkovic, I., Cruciani, S., Llovera, L., Lucas, M.C., Medina, R., Pauli, C., Heid, D., Muley, T., Schneider, M.A., Klotz, L.V., et al. (2025). Epitranscriptomic rRNA fingerprinting reveals tissue-of-origin and tumor-specific signatures. Mol Cell *85*, 177-190.e177. 10.1016/j.molcel.2024.11.014.
8. White, J., Li, Z., Sardana, R., Bujnicki, J.M., Marcotte, E.M., and Johnson, A.W. (2008). Bud23 methylates G1575 of 18S rRNA and is required for efficient nuclear export of pre-40S subunits. Mol Cell Biol *28*, 3151-3161. 10.1128/MCB.01674-07.
9. Zorbas, C., Nicolas, E., Wacheul, L., Huvelle, E., Heurgué-Hamard, V., and Lafontaine, D.L. (2015). The human 18S rRNA base methyltransferases DIMT1L and WBSCR22-TRMT112 but not rRNA modification are required for ribosome biogenesis. Mol Biol Cell *26*, 2080-2095. 10.1091/mbc.E15-02-0073.
10. Õunap, K., Käsper, L., Kurg, A., and Kurg, R. (2013). The human WBSCR22 protein is involved in the biogenesis of the 40S ribosomal subunits in mammalian cells. PLoS One *8*, e75686. 10.1371/journal.pone.0075686.
11. Baxter, M., Voronkov, M., Poolman, T., Galli, G., Pinali, C., Goosey, L., Knight, A., Krakowiak, K., Maidstone, R., Iqbal, M., et al. (2020). Cardiac mitochondrial function depends on BUD23 mediated ribosome programming. eLife *9*. 10.7554/eLife.50705.
12. Eguchi, J., Wang, X., Yu, S., Kershaw, E.E., Chiu, P.C., Dushay, J., Estall, J.L., Klein, U., Maratos-Flier, E., and Rosen, E.D. (2011). Transcriptional control of adipose lipid handling by IRF4. Cell Metab *13*, 249-259. 10.1016/j.cmet.2011.02.005.
13. Ono-Moore, K.D., Rutkowsky, J.M., Pearson, N.A., Williams, D.K., Grobe, J.L., Tolentino, T., Lloyd, K.C.K., and Adams, S.H. (2020). Coupling of energy intake and energy expenditure across a temperature spectrum: impact of diet-induced obesity in mice. Am J Physiol Endocrinol Metab *319*, E472-e484. 10.1152/ajpendo.00041.2020.

14. Newman, A.M., Liu, C.L., Green, M.R., Gentles, A.J., Feng, W., Xu, Y., Hoang, C.D., Diehn, M., and Alizadeh, A.A. (2015). Robust enumeration of cell subsets from tissue expression profiles. Nature methods *12*, 453-457. 10.1038/nmeth.3337.
15. Sárvári, A.K., Van Hauwaert, E.L., Markussen, L.K., Gammelmark, E., Marcher, A.B., Ebbesen, M.F., Nielsen, R., Brewer, J.R., Madsen, J.G.S., and Mandrup, S. (2021). Plasticity of Epididymal Adipose Tissue in Response to Diet-Induced Obesity at Single-Nucleus Resolution. Cell Metab *33*, 437-453.e435. 10.1016/j.cmet.2020.12.004.
16. Haag, S., Kretschmer, J., and Bohnsack, M.T. (2015). WBSCR22/Merm1 is required for late nuclear pre-ribosomal RNA processing and mediates N7-methylation of G1639 in human 18S rRNA. Rna *21*, 180-187. 10.1261/rna.047910.114.
17. Black, J.J., Sardana, R., Elmir, E.W., and Johnson, A.W. (2020). Bud23 promotes the final disassembly of the small subunit Processome in Saccharomyces cerevisiae. PLoS Genet *16*, e1009215. 10.1371/journal.pgen.1009215.
18. Benador, I.Y., Veliova, M., Mahdaviani, K., Petcherski, A., Wikstrom, J.D., Assali, E.A., Acín-Pérez, R., Shum, M., Oliveira, M.F., Cinti, S., et al. (2018). Mitochondria Bound to Lipid Droplets Have Unique Bioenergetics, Composition, and Dynamics that Support Lipid Droplet Expansion. Cell Metab *27*, 869-885.e866. 10.1016/j.cmet.2018.03.003.
19. Freyre, C.A.C., Rauher, P.C., Ejsing, C.S., and Klemm, R.W. (2019). MIGA2 Links Mitochondria, the ER, and Lipid Droplets and Promotes De Novo Lipogenesis in Adipocytes. Mol Cell *76*, 811-825.e814. 10.1016/j.molcel.2019.09.011.
20. Fan, H., and Tan, Y. (2024). Lipid Droplet-Mitochondria Contacts in Health and Disease. Int J Mol Sci *25*. 10.3390/ijms25136878.
21. Schuler, M., Dierich, A., Chambon, P., and Metzger, D. (2004). Efficient temporally controlled targeted somatic mutagenesis in hepatocytes of the mouse. Genesis *39*, 167-172. 10.1002/gene.20039.
22. Galloway, C.A., and Yoon, Y. (2013). Mitochondrial morphology in metabolic diseases. Antioxid Redox Signal *19*, 415-430. 10.1089/ars.2012.4779.
23. Ngo, J., Choi, D.W., Stanley, I.A., Stiles, L., Molina, A.J.A., Chen, P.H., Lako, A., Sung, I.C.H., Goswami, R., Kim, M.Y., et al. (2023). Mitochondrial morphology controls fatty acid utilization by changing CPT1 sensitivity to malonyl-CoA. Embo j *42*, e111901. 10.15252/embj.2022111901.
24. Janich, P., Arpat, A.B., Castelo-Szekely, V., Lopes, M., and Gatfield, D. (2015). Ribosome profiling reveals the rhythmic liver translatome and circadian clock regulation by upstream open reading frames. Genome Res *25*, 1848-1859. 10.1101/gr.195404.115.
25. Rath, S., Sharma, R., Gupta, R., Ast, T., Chan, C., Durham, T.J., Goodman, R.P., Grabarek, Z., Haas, M.E., Hung, W.H.W., et al. (2021). MitoCarta3.0: an updated mitochondrial proteome now with sub-organelle localization and pathway annotations. Nucleic Acids Res *49*, D1541-d1547. 10.1093/nar/gkaa1011.
26. Hochstoeger, T., and Chao, J.A. (2024). Towards a molecular understanding of the 5'TOP motif in regulating translation of ribosomal mRNAs. Semin Cell Dev Biol *154*, 99-104. 10.1016/j.semcdb.2023.06.001.
27. Atger, F., Gobet, C., Marquis, J., Martin, E., Wang, J., Weger, B., Lefebvre, G., Descombes, P., Naef, F., and Gachon, F. (2015). Circadian and feeding rhythms differentially affect rhythmic mRNA transcription and translation in mouse liver. Proc Natl Acad Sci U S A *112*, E6579-6588. 10.1073/pnas.1515308112.
28. Sinturel, F., Gerber, A., Mauvoisin, D., Wang, J., Gatfield, D., Stubblefield, J.J., Green, C.B., Gachon, F., and Schibler, U. (2017). Diurnal Oscillations in Liver Mass and Cell Size Accompany Ribosome Assembly Cycles. Cell *169*, 651-663.e614. 10.1016/j.cell.2017.04.015.
29. Gobet, C., and Naef, F. (2022). Ribo-DT: An automated pipeline for inferring codon dwell times from ribosome profiling data. Methods *203*, 10-16. 10.1016/j.ymeth.2021.10.004.

30. Petrychenko, V., Yi, S.H., Liedtke, D., Peng, B.Z., Rodnina, M.V., and Fischer, N. (2025). Structural basis for translational control by the human 48S initiation complex. Nat Struct Mol Biol *32*, 62-72. 10.1038/s41594-024-01378-4.
31. Kolitz, S.E., and Lorsch, J.R. (2010). Eukaryotic initiator tRNA: finely tuned and ready for action. FEBS Lett *584*, 396-404. 10.1016/j.febslet.2009.11.047.
32. von Heijne, G. (1986). Mitochondrial targeting sequences may form amphiphilic helices. Embo j *5*, 1335-1342. 10.1002/j.1460-2075.1986.tb04364.x.
33. Brito Querido, J., Díaz-López, I., and Ramakrishnan, V. (2024). The molecular basis of translation initiation and its regulation in eukaryotes. Nat Rev Mol Cell Biol *25*, 168-186. 10.1038/s41580-023-00624-9.
34. Zhong, H., Janer, A., Khalimonchuk, O., Antonicka, H., Shoubridge, E.A., and Barrientos, A. (2023). BOLA3 and NFU1 link mitoribosome iron-sulfur cluster assembly to multiple mitochondrial dysfunctions syndrome. Nucleic Acids Res *51*, 11797-11812. 10.1093/nar/gkad842.
35. Fujisawa, K., Wakazaki, M., Matsuzaki, A., Matsumoto, T., Yamamoto, N., Noma, T., and Takami, T. (2022). Adenylate Kinase Isozyme 3 Regulates Mitochondrial Energy Metabolism and Knockout Alters HeLa Cell Metabolism. Int J Mol Sci *23*. 10.3390/ijms23084316.
36. Tucker, E.J., Wanschers, B.F., Szklarczyk, R., Mountford, H.S., Wijeyeratne, X.W., van den Brand, M.A., Leenders, A.M., Rodenburg, R.J., Reljić, B., Compton, A.G., et al. (2013). Mutations in the UQCC1-interacting protein, UQCC2, cause human complex III deficiency associated with perturbed cytochrome b protein expression. PLoS Genet *9*, e1004034. 10.1371/journal.pgen.1004034.
37. Nechushtai, R., Rowland, L., Karmi, O., Marjault, H.B., Nguyen, T.T., Mittal, S., Ahmed, R.S., Grant, D., Manrique-Acevedo, C., Morcos, F., et al. (2024). CISD3/MiNT is required for complex I function, mitochondrial integrity, and skeletal muscle maintenance. Proc Natl Acad Sci U S A *121*, e2405123121. 10.1073/pnas.2405123121.
38. Missaglia, S., Tavian, D., and Angelini, C. (2021). ETF dehydrogenase advances in molecular genetics and impact on treatment. Crit Rev Biochem Mol Biol *56*, 360-372. 10.1080/10409238.2021.1908952.
39. Schmidt, A.F., Finan, C., Gordillo-Marañón, M., Asselbergs, F.W., Freitag, D.F., Patel, R.S., Tyl, B., Chopade, S., Faraway, R., Zwierzyna, M., and Hingorani, A.D. (2020). Genetic drug target validation using Mendelian randomisation. Nat Commun *11*, 3255. 10.1038/s41467-020-16969-0.
40. Sanderson, E., Glymour, M.M., Holmes, M.V., Kang, H., Morrison, J., Munafò, M.R., Palmer, T., Schooling, C.M., Wallace, C., Zhao, Q., and Smith, G.D. (2022). Mendelian randomization. Nat Rev Methods Primers *2*. 10.1038/s43586-021-00092-5.
41. Verma, A., Huffman, J.E., Rodriguez, A., Conery, M., Liu, M., Ho, Y.L., Kim, Y., Heise, D.A., Guare, L., Panickan, V.A., et al. (2024). Diversity and scale: Genetic architecture of 2068 traits in the VA Million Veteran Program. Science *385*, eadj1182. 10.1126/science.adj1182.
42. Murphy, J.C., Harrington, E.M., Schumann, S., Vasconcelos, E.J.R., Mottram, T.J., Harper, K.L., Aspden, J.L., and Whitehouse, A. (2023). Kaposi's sarcoma-associated herpesvirus induces specialised ribosomes to efficiently translate viral lytic mRNAs. Nat Commun *14*, 300. 10.1038/s41467-023-35914-5.
43. Peng, H., Chen, B., Wei, W., Guo, S., Han, H., Yang, C., Ma, J., Wang, L., Peng, S., Kuang, M., and Lin, S. (2022). N(6)-methyladenosine (m(6)A) in 18S rRNA promotes fatty acid metabolism and oncogenic transformation. Nat Metab *4*, 1041-1054. 10.1038/s42255-022-00622-9.
44. Liu, P., Huang, F., Lin, P., Liu, J., Zhou, P., Wang, J., Sun, H., Xing, F., and Ma, H. (2025). Histidine metabolism drives liver cancer progression via immune microenvironment modulation through metabolic reprogramming. J Transl Med *23*, 262. 10.1186/s12967-025-06267-y.

45. Huang, T., Jiao, B., Luo, Z., Zhang, X., and Wang, Z. (2024). BUD23 promote the cell proliferation ability by affecting the PPAR signaling pathways: evidence from the online dataset and cell experiment. Discov Oncol *15*, 750. 10.1007/s12672-024-01648-z.
46. Jangani, M., Poolman, T.M., Matthews, L., Yang, N., Farrow, S.N., Berry, A., Hanley, N., Williamson, A.J., Whetton, A.D., Donn, R., and Ray, D.W. (2014). The methyltransferase WBSCR22/Merm1 enhances glucocorticoid receptor function and is regulated in lung inflammation and cancer. J Biol Chem *289*, 8931-8946. 10.1074/jbc.M113.540906.
47. Kozel, B.A., Barak, B., Kim, C.A., Mervis, C.B., Osborne, L.R., Porter, M., and Pober, B.R. (2021). Williams syndrome. Nat Rev Dis Primers *7*, 42. 10.1038/s41572-021-00276-z.
48. Robinson, M.D., McCarthy, D.J., and Smyth, G.K. (2010). edgeR: a Bioconductor package for differential expression analysis of digital gene expression data. Bioinformatics *26*, 139-140. 10.1093/bioinformatics/btp616.
49. Snieckute, G., Genzor, A.V., Vind, A.C., Ryder, L., Stoneley, M., Chamois, S., Dreos, R., Nordgaard, C., Sass, F., Blasius, M., et al. (2022). Ribosome stalling is a signal for metabolic regulation by the ribotoxic stress response. Cell Metab *34*, 2036-2046.e2038. 10.1016/j.cmet.2022.10.011.
50. McGlincy, N.J., and Ingolia, N.T. (2017). Transcriptome-wide measurement of translation by ribosome profiling. Methods *126*, 112-129. 10.1016/j.ymeth.2017.05.028.
51. Arpat, A.B., Liechti, A., De Matos, M., Dreos, R., Janich, P., and Gatfield, D. (2020). Transcriptome-wide sites of collided ribosomes reveal principles of translational pausing. Genome Res *30*, 985-999. 10.1101/gr.257741.119.
52. Granat, R., Donnellan, A., Heflin, M., Lyzenga, G., Glasscoe, M., Parker, J., Pierce, M., Wang, J., Rundle, J., and Ludwig, L.G. (2021). Clustering Analysis Methods for GNSS Observations: A Data-Driven Approach to Identifying California's Major Faults. Earth Space Sci *8*, e2021EA001680. 10.1029/2021ea001680.
53. Love, M.I., Huber, W., and Anders, S. (2014). Moderated estimation of fold change and dispersion for RNA-seq data with DESeq2. Genome Biol *15*, 550. 10.1186/s13059-014-0550-8.
54. Gobet, C., Weger, B.D., Marquis, J., Martin, E., Neelagandan, N., Gachon, F., and Naef, F. (2020). Robust landscapes of ribosome dwell times and aminoacyl-tRNAs in response to nutrient stress in liver. Proc Natl Acad Sci U S A *117*, 9630-9641. 10.1073/pnas.1918145117.
55. Heath, R.B., Karpe, F., Milne, R.W., Burdge, G.C., Wootton, S.A., and Frayn, K.N. (2003). Selective partitioning of dietary fatty acids into the VLDL TG pool in the early postprandial period. J Lipid Res *44*, 2065-2072. 10.1194/jlr.M300167-JLR200.
56. Johansson, M.U., Zoete, V., Michielin, O., and Guex, N. (2012). Defining and searching for structural motifs using DeepView/Swiss-PdbViewer. BMC Bioinformatics *13*, 173. 10.1186/1471-2105-13-173.

Material and Methods

Animals

AdipoqCREBud23fl/fl (AdKO), *UCP1CREBud23fl/fl* (UCPKO) and *Alb^{CreERT2}Bud23$^{fl/fl}$* (LivKO) mice were generated by crossing AdipoqCre (JAX laboratory, Strain #:028020), UCP1Cre (JAX laboratory, Strain #:024670) and AlbCreERT2 (given by Prof. Pierre Chambon, GIE-CERBM (IGBMC)) respectively, with Bud23flox/flox (generated at the University of Manchester (UK) [11]. In all studies, CRE-negative littermates (Bud23$^{fl/fl}$) were used as controls (AdWT; UCPWT; LivWT). All mice were group-housed in 12:12 light/dark cycles, under controlled temperature (22±2C) and humidity with ad libitum access to standard laboratory chow, unless stated otherwise. All studies used both male and female mice, unless otherwise stated. All experiments were carried out in accordance with the Animals (Scientific Procedures) Act 1986 (UK) under Home Office Project License PDC3CD59F (University of Oxford) and PP1136445 (University of Manchester) and approval from local ethical review bodies.

In vivo treatmenst and studies

Transgene induction: LivWT and LivKO mice were treated daily with tamoxifen (Sigma, T5648) for 5 days (i.p., 0.1mg/day in sesame oil, Sigma S3547).

High fat diet challenge: Adult mice (10-13 weeks of age) were given ad libitum access to a high fat diet (60% energy from fat, DIO Rodent Purified Diet, IPS Ltd) for a period of 9-12 weeks.

Metabolic phenotyping: Body composition was assessed using an EchoMRI (Echo Medical Systems, E26-258-MT). Physiological (metabolic gas exchange) and behavioural (food and water intake, locomotor activity) rhythms were measured using the Phenomaster indirect calorimetry system (TSE Systems). Mice were individually housed and acclimatised for 24hr. with O2 consumption (VO2), CO2 production (VCO2) and energy expenditure (EE) recorded every 2 min for >72 hr. RER was derived from these measures (VCO2/VO2).

Cold and thermoneutrality challenges: For cold challenge, mice (~13 weeks of age) were individually housed within a Phenomaster system, and following >2 days acclimatisation were exposed to an abrupt drop in ambient temperature to 4°C for 6 hours. For thermoneutrality studies, group housed mice were placed ~29°C (+/- 1°C) ambient temperature for 7 weeks.

Insulin Tolerance Test: Blood glucose was measured from tail blood using the Aviva Accuchek meter (Roche). For the insulin tolerance test, mice were fasted from ZT0, then injected with 0.75 IU/kg human recombinant insulin (I2643, Sigma-Aldrich) at ZT6 (time '0 min').

Thermal imaging & Body temperature. BAT temperature of free moving Ad^{WT} and Ad^{KO} mice were measured using a thermal camera (Flir). Mice were shaved to expose the interscapular region >2 d prior to thermal imaging to avoid stress-induced BAT activity. Average temperature was calculated using Flir Tools software, where the average temperature was measured from a minimum of four images per mouse. Rectal temperature of unanaesthetised AD mice was measured using mouse rectal probe (RET-3, Type T Thermocouple, World Precision Instruments) connected to a BAT-12 Microprobe Thermometer (Physitemp Instruments). Recording of body temperature and activity was carried out via surgically implanted radiotelemetry devices (TA-F10, Data Sciences International). Following >10days recovery, body temperature was recorded every 5 min for >5 d.

Labelled substrates study. Male adult AD^{WT} / AD^{KO} animals were given deuterated water (^2H_2O) (CK Isotopes, Ibstock,UK) in the drinking water (25%vol/vol, ad libitum) for 48 hrs. After this period, they were fasted for 4 hours and then received an oral bolus of labelled glucose (D-glucose; U-13C6, Cambridge Isotope Laboratories, INC). Tissues were collected 2 hrs post-glucose administration.

Primary cell culture

Adipose tissue fractionation: Brown adipose tissue (BAT) was collected and washed in PBS supplemented with amphotericin B from mice aged between 9-14 wks old. The tissue was minced and digested in 1.5mg/ml collagenase H (25 min, shaking incubator 170rpm, 37°C). Collagenase solution was neutralised with DMEM (containing 20% FBS, 1% PS, 5µg/ml amphotericin B) and passed through a 100µm mesh filter. Cells were centrifuged (250g, RT 8 min) to separate the stromal vascular fraction (SVF) from the floating mature adipocyte layer. The SVF was collected and cultured until confluent. For BAT differentiation cells were plated at 50,000 cells/well, cultured for 3d prior to treatment with the differentiation cocktail (IBMX 0.5mM, indomethacin 0.125mM, dexamethasone 1µM, rosiglitazone 2.8µM, T3 1nM, insulin, 20nM) in DMEM (with 20% FBS, 1% PS). 5d post-plating, media was replaced with DMEM (with rosiglitazone 2.8µM, T3 1nM, insulin 20nM, 10% FBS, 1% PS). From 7d post-plating, media was replaced with Rosiglitazone (2.8µM) and Insulin (20nM) in DMEM + 10% FBS + 1% PS.

For gonadal white adipose tissue (gWAT) tissue was washed in PBS supplemented with amphotericin B, then minced and digested and washed as above. The gWAT SVF pellet was then collected and resuspended in DMEM (glutamax) + 20% FBS + 1% PS prior to isolation with the adipose tissue progenitor isolation kit (Miltenyi Biotec) according to manufacturer's instructions. The purified progenitor population was cultured for 24 hrs in DMEM (20% FBS, 1% PS) before being replaced and maintained in DMEM (20% FBS only). Once confluent, cells were plated at 50,000 cells/well. Differentiation was triggered 3d later using differentiation cocktail (IBMX 0.5mM, Dexamethasone 1µM, Rosiglitazone 4µg/ml, insulin 5µg/ml in DMEM, 20% FBS). On day 6 and day 8 post-plating, media was replaced with DMEM (20% FBS, 5µg/ml insulin).

Oil Red O and BODIPY/Hoechst staining. Differentiated cells were stained using Hoechst 33342, Trihydrochloride, Trihydrate and BODIPY 493/503 (4,4-Difluoro-1,3,5,7,8-Pentamethyl-4-Bora-3a,4a-Diaza-s-Indacene; Fisher Scientific UK Ltd.) at 1:2000. Images were taken using the EVOS™ M5000 Imaging system. For Oil Red O staining (ORO), cells were washed in PBS and fixed in 10% Formalin (Merck Life Science UK Limited) for 30 mins. Cells were rinsed with deionised water and incubated with 60% isopropanol for 5 min before being stained with ORO solution for 15 minutes. Cells were wrinsed with deionised water before being imaged on the EVOS™ M5000 Imaging system. Following imaging, the ORO was quantified by the addition of 100% isopropanol for 5 minutes. The absorbance of the extracted ORO solution was measured at 492nm on a plate reader.

Mature adipocyte studies. Following a method adapted from Collins et al., 2010, gWAT was collected from adult mice and washed in Hanks' Balanced Salt Solution (Sigma). Next, tissue was minced and digested in 1 mg/ml collagenase (Collagenase H, Sigma) for 30 min in a shaking incubator at 170 rpm, 37°C. The sample was then centrifuged at 1000 rpm for 5 min at 4°C. MA (floating layer) and stromal vascular fraction (SVF) (cell pellet) were collected

separately, lysed in TRIzol Reagent (Invitrogen), and stored at −80°C before proceeding to RNA extraction. To remove excess lipid from MA fractions, samples were centrifuged (full speed, 5 min, room temperature) prior to chloroform addition. RNA extraction was then carried out as per the manufacturer's TRIzol protocol, up to the stage of removing the isopropranol phase, which was transferred to Reliaprep columns (Promega) for on-column DNase treatment, clean-up, and elution as per manufacturer's protocol.

Cell culture RNA extraction. RNA was extracted from cells using the ReliaPrep™ RNA cell mini prep system (Promega UK Ltd.) following the manufacturer's instructions. Samples were DNAse treated during the extraction procedure. RNA was eluted from the column in a final volume of 15µL and RNA concentration and purity was assessed using a NanoDrop 2000c UV/IV Spectrophotometer.

RNA extraction (tissue)

Total RNA was isolated by using Trizol Reagent (Invitrogen; Carlsbad, CA, USA) according to the manufacturer's protocol (RNA was precipitated with chloroform and isopropanol, washed with 75% ethanol, and finally dissolved in RNase-free water). RNA concentration and purity was assessed using a NanoDrop 2000c UV/IV Spectrophotometer. Before the retrotranscription, RNA was DNAse treated using RQ1 DNAse (Promega) following manufacturer's protocol.

RT-PCR. Samples were DNase-treated (RQ1 RNase-Free DNase, Promega, Madison, WI) prior to cDNA conversion High Capacity RNA-to-cDNA kit (Applied Biosystems). qPCR was performed using a GoTaq qPCR Master Mix (Promega, Madison, WI) and primers listed in Appendix Adipocyte NR1D1 dictates adipose tissue expansion during obesity using a Step One Plus (Applied Biosystems) qPCR machine. Relative quantities of gene expression were determined using the [delta][delta] Ct method and normalised with the use of a geometric mean of the housekeeping genes Hprt, Ppib, and Actb. The fold difference of expression was calculated relative to the values of control groups.

RNA-Sequencing

BAT: RNA was extracted from BAT using the SV Total RNA Isolation System (Promega) according to manufacturer's instructions. RNA yield was quantified by TapeStation (Agilent), to ensure it was of sufficient quality for sequencing. Library preparation and sequencing for the Illumina HiSeq 4000 platform were performed by Novogene. Raw FASTQ files were processed through a standard pipeline by Novogene to generate a list of counts. Gene lists were analysed for differential expression using a combination of techniques, including edgeR [48].

gWAT. Adipose tissue was collected from adult male mice (13 wks of age) at ZT8 and flash-frozen. Total RNA was extracted and DNase-treated as described above. Biological replicates were taken forward individually to library preparation and sequencing. For library preparation, total RNA was submitted to the Genomic Technologies Core Facility (GTCF). Quality and integrity of the RNA samples were assessed using a 2200 TapeStation (Agilent Technologies) and then libraries generated using the TruSeq Stranded mRNA assay (Illumina, Inc) according to the manufacturer's protocol. Briefly, total RNA (0.1–4 µg) was used as input material from which polyadenylated mRNA was purified using poly-T, oligo-attached, magnetic beads. The mRNA was then fragmented using divalent cations under elevated temperature and then reverse-transcribed into first strand cDNA using random primers. Second strand cDNA was then synthesised using DNA Polymerase I and RNase H. Following a single 'A' base addition,

adapters were ligated to the cDNA fragments, and the products then purified and enriched by PCR to create the final cDNA library. Adapter indices were used to multiplex libraries, which were pooled prior to cluster generation using a cBot instrument. The loaded flow cell was then paired-end sequenced (76 + 76 cycles, plus indices) on an Illumina HiSeq4000 instrument. Finally, the output data was demultiplexed (allowing one mismatch) and BCL-to-Fastq conversion performed using Illumina's bcl2fastq software, version 2.17.1.14.

Genomic DNA extraction and Mitochondria Copy Number analysis

Genomic DNA (gDNA) was extracted using phenol-chloroform. Tissue was homogenized in TE buffer and incubate at 55°C for 3 hours with proteinase K and 20% SDS. After that, 1 volume of phenol:chloroform:isoamyl alcohol (25:24:1; Thermo Fisher) per sample was added and vortexed for 20 seconds. Samples were transfered into phase lock tubes (Qiagen) prior to centrifugation at 16,000g for 5 mins. The aqueous phase was carefully removed and transferred to a fresh tube. 1 µl GlycoBlue, half a volume of 7.5M ammonium acetate, and 2.5 volumes of 100% ethanol were added. The sample was kept at -80°C for one hour to facilitate DNA precipitation. The sample was then centrifuged at 16,000g at 4°C for 30 mins to pellet the DNA. The pellet was washed in ethanol once and left to air dry. Purified genomic DNA was resuspended in nuclease-free water.

Mitochondria Copy Number was analysed by qPCR by measuring the mitochondrial genome gen mt-ND1 and normalizing the values by genomic GAPDH.

Ribosome profiling from mouse liver samples

Livers from *Bud23*$^{fl/fl}$;*Alb*^{CreERT2} (Liv^{KO}) and age-matched *Bud23*$^{fl/fl}$ (Liv^{WT}) animals (both groups tamoxifen-treated) were collected at diurnal Zeitgeber timepoints ZT6 and ZT18 (3 male mice per genotype and timepoint) and flash-frozen in liquid nitrogen. Using ~200 mg of frozen sample per liver, tissue lysates were prepared and ribosome footprints were generated (RNase I) and purified, all according to previously described protocols as in Janich et al. [24]. An aliquot of the same lysate as for footprint generation was used to purify matching total RNA preparations, of which 1 µg was chemically fragmented for RNA-seq library preparation, also as described in Janich et al. Size-selected, fragmented RNA and footprint samples were then subjected to library preparation protocols identical to those used in our previous studies (e.g. [49]. In this protocol, sample barcodes and unique molecular identifiers (UMIs) are included in the initial adaptors ligated to the RNA molecules (similar to [50]), allowing for multiplexing at an early stage, before rRNA depletion (6 samples were multiplexed for each of the final four libraries). The amplification of the libraries was carried out using i5 and i7 indexed primers (12 PCR cycles). The libraries were sequenced on a NovaSeq6000 (Illumina).

Ribosome profiling data mapping

Read mapping was performed essentially following our published protocol [51]. Briefly, reads were trimmed from adapter sequence using cutadapt (version: 3.5; options: --match-read-wildcards --overlap 8 --discard-untrimmed --minimum-length 30) and quality filtered using fastx_toolkit (version: 0.0.14; options: -Q33 -q 30 -p 90). UMIs were extracted from each read with UMItools (version: 1.0.0git; options: extract --extract-method string --bc-pattern NNNNNNNNCCCCC --3prime --filter-cell-barcode –error-correct-cell). Then, reads where size-selected for monosome footprints (size 26 to 35). Subsequently, to estimate rRNA and tRNA contamination, reads were mapped to human and mouse rRNA and mouse tRNA databases using bowtie2 (version: 2.3.5; options: -p 2 -L 15 -k 20 --trim5 2). Reads that failed

to map to these, were then mapped to the mouse transcript database (Ensembl database v. 100). Barcode demultiplexing was carried out with UMItools (options: group --method=directional --per-cell –read-length) and deduplication with an in-house script. For each gene, only one transcript isoform was considered, namely the primary isoform based on classification by the APPRIS database (PMID 34755885). In case several transcript isoforms were annotated as primary by APPRIS, the one with the longest coding region was selected. For Ribo-Seq reads, the ribosome A-site was assumed to cover nucleotide positions 15-17, and Ribo-Seq reads were counted for each gene that overlapped with their A-site the coding region. For RNA-Seq, all reads were counted that aligned to a gene.

Data and code availability

For liver ribo-seq and matching RNA-seq data, raw sequencing data files will be deposited in NCBI's Gene Expression Omnibus (GEO) archive. The scripts for data analysis will be abailable from https://github.com/gatfieldlab/.

PCA analysis

PCA analysis was done in python3 using the scikit-learn package [52]: Scikit-learn: Machine Learning in Python, Pedregosa et al., JMLR 12, pp. 2825-2830, 2011] considering genes with any reads in at least 10 out of 12 samples. Read counts were normalized by sizefactors obtained by DESeq2 [53]. Translation efficiencies were calculated by dividing normalized Ribo-Seq read counts by normalized RNA-Seq read counts for genes with any RNA-Seq reads.

Differential expression and ribosome occupancy analysis

Differential expression and ribosome occupancy analysis was done using DESeq2 [53] considering RNA-Seq and Ribo-Seq read counts, respectively. Differential translation efficiency analysis was done in python3 considering genes with reads in all RNA-Seq and Ribo-Seq samples. An independent T-test was used to compare translation efficiencies in Bud23-KO with wildtype samples, and p-values were FDR corrected. Genes with corrected p-value < 0.05 and absolute log2-fold change > 1.5 were considered significantly differentially translated.

GO analysis and gene sets

GO enrichment analysis was done in python3 using gene ontology gene sets (downloaded from MSigDB: https://www.gsea-msigdb.org/gsea/index.jsp) with at least 50 genes. For each gene set, the proportion of genes contained in the set among significantly changed genes (in KO versus WT, based on RNA-Seq, Ribo-Seq or TE) was compared with the proportion for all genes using Fisher's exact test, and *p*-values were FDR-corrected. If all genes of a smaller gene set were contained in a larger gene set and both gene sets were significantly depleted or enriched, only the larger gene set was retained. The full list of significant gene sets is provided as Supplemental Table SXX and selected representative gene sets are shown in **Figure 5D.**

In **Figure 5 E-G**, the ribosome gene set is from the GO cellular component (CC) ontology, excluding mitochondrial ribosomal genes (Mrp genes), and the mitochondrial gene set is from MitoCarta3.0 (downloaded from https://personal.broadinstitute.org/scalvo/MitoCarta3.0/Mouse.MitoCarta3.0.xls)

Codon dwell time estimation

Codon dwell times (DTs) were estimated using the RiboDT pipeline [54], based on Ribo-Seq reads. In **Figure S6E**, DTs when assuming an interaction between P- and A-sites are shown, as well as the difference between both (KO - WT).

Meta-profile of ribosome occupancy around CDS starts and ends

For each Ribo-Seq read, the A-site was assigned to start at the nucleotide at positions 15. The number of A-sites of ribosomes were counted at each nucleotide in a region from 100 nucleotides upstream to 200 nucleotides downstream of annotated start codons and in a region from 200 nucleotides upstream to 100 nucleotides downstream of annotated stop codons. For each gene, A-site counts of different samples were normalized by their sizefactors (obtained from DESeq2), summed over all Liv^{KO} or all Liv^{WT} samples, and then z-scored relative to the profile counts for wildtype. Genes with A-site counts at more than 25 positions were considered. **Figure 5I** shows the average (line) and standard error (shaded area around line) for Liv^{KO} and Liv^{WT} samples. A one-sample t-test was used to test, at each position, if the distribution of differences of z-scored A-site counts between KO and wildtype for all genes was significantly smaller or larger than 0 (i.e. no difference). The p-values for all positions were FDR corrected and considered significant when < 0.05.

Sequence properties of transcripts and their correlation with changes in translation efficiency (TE) for specific gene regions

We quantified several sequence properties of transcripts and examined their correlation with TE fold-changes in specific gene regions: in 5' UTRs, in coding regions, and in first or last 60 nucleotides of coding regions. We considered the following transcript sequence properties: distance of start codon from mRNA 5' end (5' UTR length), number of upstream open reading frames (uORFs) in 5' UTRs starting with a AUG start codons, an in-frame stop codons, and ribosome A site occupancy, , number of uORFs starting with a (C/G/U)UG start codon, Kozak score, codon optimality score (for first 20 codons), GC content for different regions (5' UTRs, 60 nucleotides upstream or downstream of start codons or both), absolute minimum free energy (MAF) for folded RNA within 60 nucleotides upstream or downstream of start codons or 120 nucleotides surrounding start codons).

As 5' UTR length we considered two measures: the distance between the annotated start codon and the annotated mRNA 5' end, and the distance between the annotated start codon and the start of transcription as indicated by CAGE (Cap analysis of gene expression) data obtained from mouse liver by the Fantom Consortium (data downloaded from https://hgdownload.soe.ucsc.edu/gbdb/mm10/fantom5/liver%252c%2520adult%2520pregnant%2520day01.CNhs10466.508-5B2.mm10.ctss.fwd.bw and https://hgdownload.soe.ucsc.edu/gbdb/mm10/fantom5/liver%252c%2520adult%2520pregnant%2520day01.CNhs10466.508-5B2.mm10.ctss.rev.bw). In particular, we assigned the transcription start site to the position with the maximum number of CAGE reads (at least 10 reads) within the first annotated exon and 500 nucleotides upstream of it.

The codon optimality score was determined by summing up the relative abundances of codons, corresponding to each codon within the first 20 codons, where the relative codon abundances were calculated from codons in expressed genes and weighted by the gene expression level in wildtype samples.

Spearman correlations between transcript sequence properties and TE fold-changes were calculated for genes with more than 1 normalized RNA-Seq read in KO and WT, more than 10 normalized Ribo-Seq reads in KO or WT, and a ratio of normalized Ribo-Seq to RNA-Seq

reads larger than 0.5 for KO or WT. As several sequence properties correlated across transcripts, we selected representative sequence properties.

Linear regression model to explain TE FCs with sequence properties

Linear regression was used to select gene sequence properties that together contribute to explaining the variance in TE FC and to quantify the total fraction of the variance explained by these combined gene sequence properties. To select contributing sequence properties, we performed a forward feature selection procedure, where in each step the sequence property maximizing the model correlation with TE FC was added. We used a five-fold cross-validation to evaluate the model performances, with regression coefficients being estimated on 80% of the data and correlations of the parametrized models with TE FCs being evaluated on the remaining 20% of the data. Splitting of the data was random and repeated 50 times. A new gene sequence property was added to the model if it increased the explained variance of TE FCs by at least 1% compared to the explained variance by the previous model.

Stable isotope analysis/ Gas chromatography

The Folch chloroform-methanol (2:1; v/v) method was used to extract total lipid from tissue lysates (PMID – 13428781). Solid-phase extraction was used to separate lipid fractions and fatty acid methyl esters (FAMEs) prepared as previously described [55]. Deuterium incorporation from $^{2}H_2O$ in plasma water (Finnigan GasBench II; Thermo Fisher Scientific, Paisley, UK). Tissue palmitate 13C (from U136 glucose) and D2 (from D2O) enrichment was determined by GC-mass spectrometry (GC-MS) (Agilent Technologies; CA, USA)with monitoring ions with mass-to-charge ratios (m/z) of 270 (M+0), 271 (M+1) and 272 (M+2).

Western blot

Total protein was isolated from gWAT and liver using protein extraction RIPA supplemented with protease and phosphatase inhibitors in a tissue homogenizer. Protein quantification was performed following the Bradford method. Protein lysates were subjected to SDS-PAGE, electrotransferred and blocked with milk/BSA. Primary antibodies were incubated overnight at 4C: DGAT2, FAS, ATGL, LPL. Fluorescence secondary antibodies were incubated 1 hour at room temperature and imagines were taken using Biorad Gel Doc system. Band signal was quantified by densitometry using ImageJ 1.33 software, values were expressed in relation to b-actin/ total protein ponceau. Representative images for all proteins are shown.

Histology

Haematoxylin and Eosin (H&E) staining was carried out on paraffin embedded sections using the Leica ST5010 Autostainer XL. Images were acquired on a 3D-Histech Pannoramic-250 microscope slide-scanner using a 20x/ 0.80 Plan Apochromat objective (Zeiss). Snapshots of the slide-scans were taken using the SlideViewer software (3D-Histech). Further imaging was also carried out on the Zeiss AX10. Adipocyte diameter was quantified using ImageJ and the Adiposoft plugin version 1.16.

Proteomics - Mass Spectrometry

Adipose tissue homogenates were processed for in-solution protein digestion. Proteins were reduced with 5 mM DTT (60 min, room temperature) and alkylated with 20 mM iodoacetamide (60 min). Proteins were precipitated using methanol/chloroform, and pellets were resuspended in 6 M urea, then diluted to <1 M prior to protein quantification (Bradford assay).

Samples were digested overnight at 37°C with trypsin (1:50 enzyme-to-protein ratio) and desalted using Pierce C18 tips. Peptides were analysed by LC-MS/MS using an UltiMate 3000 RSLC system coupled to a Q Exactive HF mass spectrometer (Thermo Scientific). Separation was performed on a 75 mm × 250 µm, 1.7 µm CSH C18 column over a 120-minute multistep acetonitrile/formic acid gradient at 300 nL/min. MS1 scans were acquired at 120,000 resolution with a 300–1750 m/z window, followed by data-dependent MS2 scans (top 12 precursors, resolution 60,000, dynamic exclusion 15 s). Normalised collision energy was stepped around 28, and ionisation was set at 1,900 V. Mass spectra were analysed using MaxQuant version 1.6.0.16

Blood biochemistry

Blood serum was acquired via cardiac puncture. Blood was allowed to clot at room temperature for 30 mins, before centrifugation at 2,000g for 10 mins. Serum was collected and the pellet discarded. Metabolites (including glucose, glycerol, NEFA, TG, lactate, cholesterol, 3-OHB, CRP, Urea, HDL) were assessed via ILab 650 Automatic Biochemistry Analyzer Clinical Chemistry System.

Adiponectin ELISA

Adiponectin in cell culture supernatant was measured using the mouse Adiponectin/Acrp30 DuoSet ELISA (Bio-Techne Ltd.) according to manufacturer's instructions. Cell culture supernatant was diluted 1:500 to fall within the range of the assay.

Bio-Plex

Serum samples were analysed using the Bio-Plex Pro Mouse Diabetes 8-Plex assay kit (171F7001M, Bio-Rad Laboratories Ltd) and the Bio-Plex 200 system (Bio-Rad Laboratories Ltd.). The assay was run according to the manufacturer's instructions and at the recommended dilution for serum samples.

Triglyceride assay

Triglyceride in tissue lysates was measured using a Cayman's Triglyceride calorimetric assay (CAY700190-96 wells, Cambridge Bioscience Ltd.) according to the manufacturer's instructions. Lysates were prepared from ~100mg pieces of liver homogenised in lysing matrix D tubes (MP Biomedicals) with NP40 substitute assay reagent supplemented with a cOmplete mini EDTA protease inhibitor tablet (Merck Life Science UK Limited). Lysates were diluted 1:3 to fall within the range of the assay.

Electron Microscopy

Livers were dissected from adult mice, after PBS perfusion and immersed in fixative solution (2.5% glut/4% formaldehyde) for 1 hr at room temperature and then kept at 4C until processing.

Fixed samples were processed with microwave assistance using a Leica AMW according to the following steps. Samples were washed with buffer (0.1 M sodium cacodylate buffer pH 7.2), stained with 1% osmium tetroxide and 1.5% potassium ferrocyanide in buffer, then rinsed with MilliQ water. Samples were further stained with 2% uranyl acetate in water, rinsed again with MilliQ water, then dehydrated through an ethanol series (30%, 50%, 70%, 90%, 95% and absolute ethanol). Samples were then infiltrated with 25%, 50%. 75% and finally 100% low viscosity resin (TAAB) in ethanol. Samples were removed from the microwave processor and submerged in fresh 100% resin, then placed on a rotator overnight. Samples were incubated

on the rotator for the following 4 days, with changes into fresh resin twice per day. The samples were embedded on the afternoon of the final day and polymerised at 60°C for 48 hours. Sections of 90 nm were cut from the resin blocks using a Leica UC7 Ultramicrotome and collected onto 3 mm copper grids. The sections were then post-stained with lead citrate and imaged using a JEOL Flash 120kV TEM equipped with a Gatan Rio camera. Analysis was done using Image J.

Structural models

For structural models in Figure 5K and S7, PDB entries_8pj1-5 were loaded in Swiss-PdbViewer [56] and the m^7G1639 methyl group was added by superposing the guanine aromatic ring of pdb entry 5H3T chain A:MGT801 onto PDB entries 8pj1-5 G1639 guanine aromatic rings. The molecular surface of 18S rRNA (chain A) was computed excluding G1639 to show the space available to perfectly accomodate m^7G1639. Chains e (40S ribosomal protein S25 / eS25), f (40S ribosomal protein S18 / uS13), w (initiator Met-tRNA) and 7 (mRNA) were drawn in purple, teal, dark green, yellow ribbon, respectively.

Data analysis and statistics

Data are expressed as mean SEM. Error bars represent SEM. Statistical significance was determined by Student t test (when two groups were compared), ANOVA (when more than two groups were compared) followed by post hoc Bonferroni test. $P < 0.05$ was considered significant.

Figure 1. Loss of Bud23 function drives profound metabolic phenotype and shift in body composition.

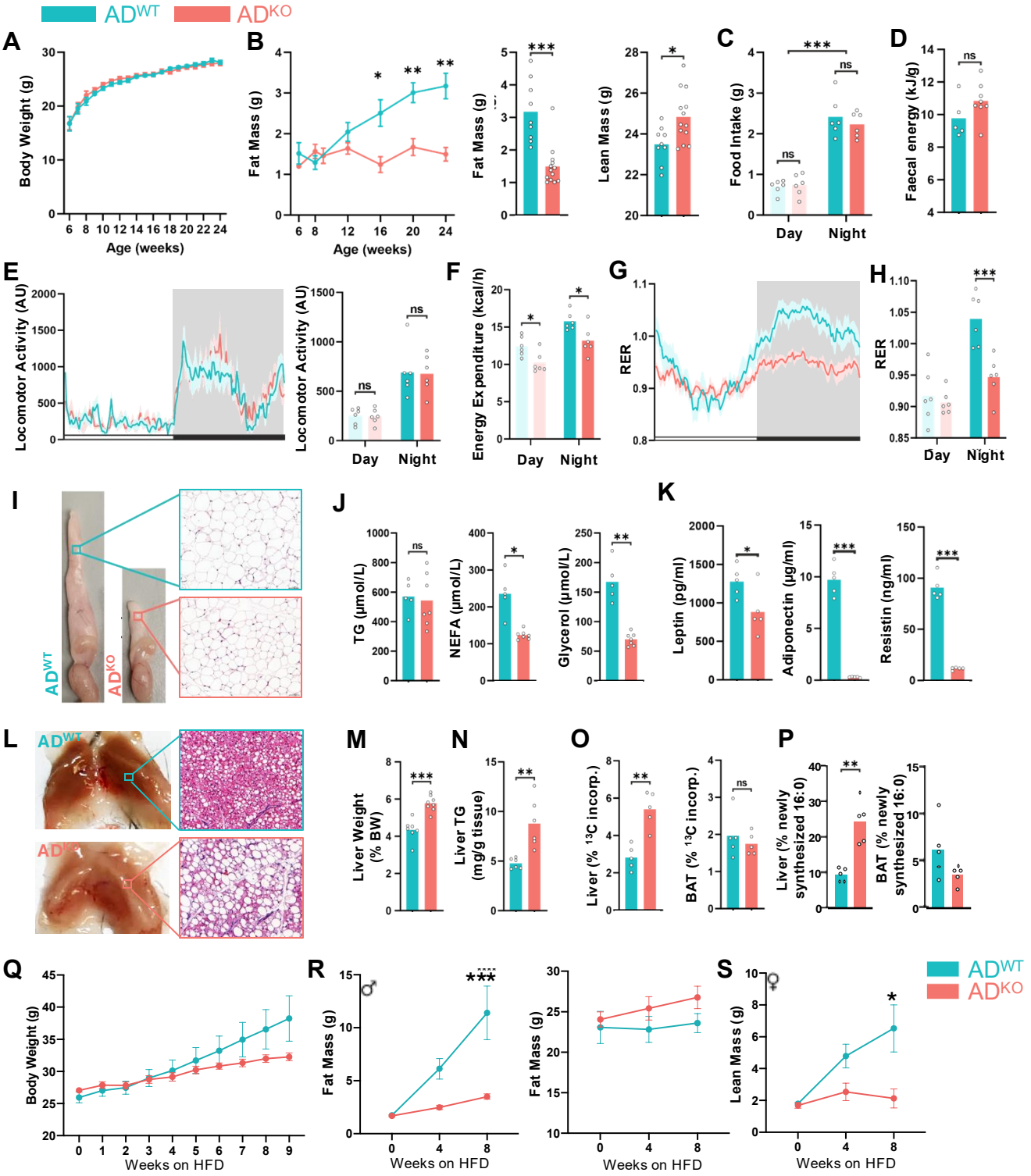

Figure 2. Bud23 is required for normal white adipocyte function

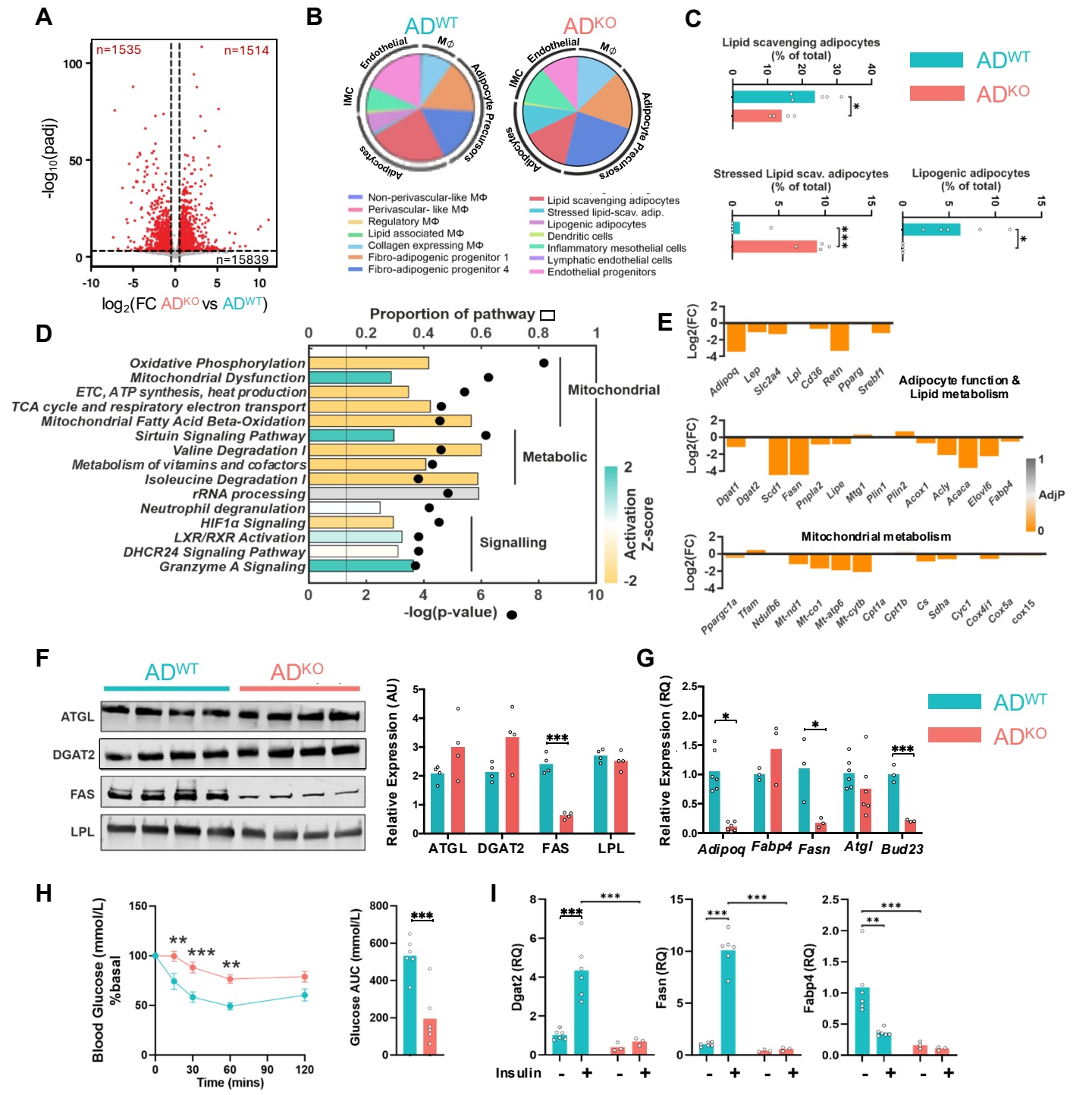

Figure 3. Bud23 directs brown adipose tissue morphology, lipid metabolism and mitochondrial function.

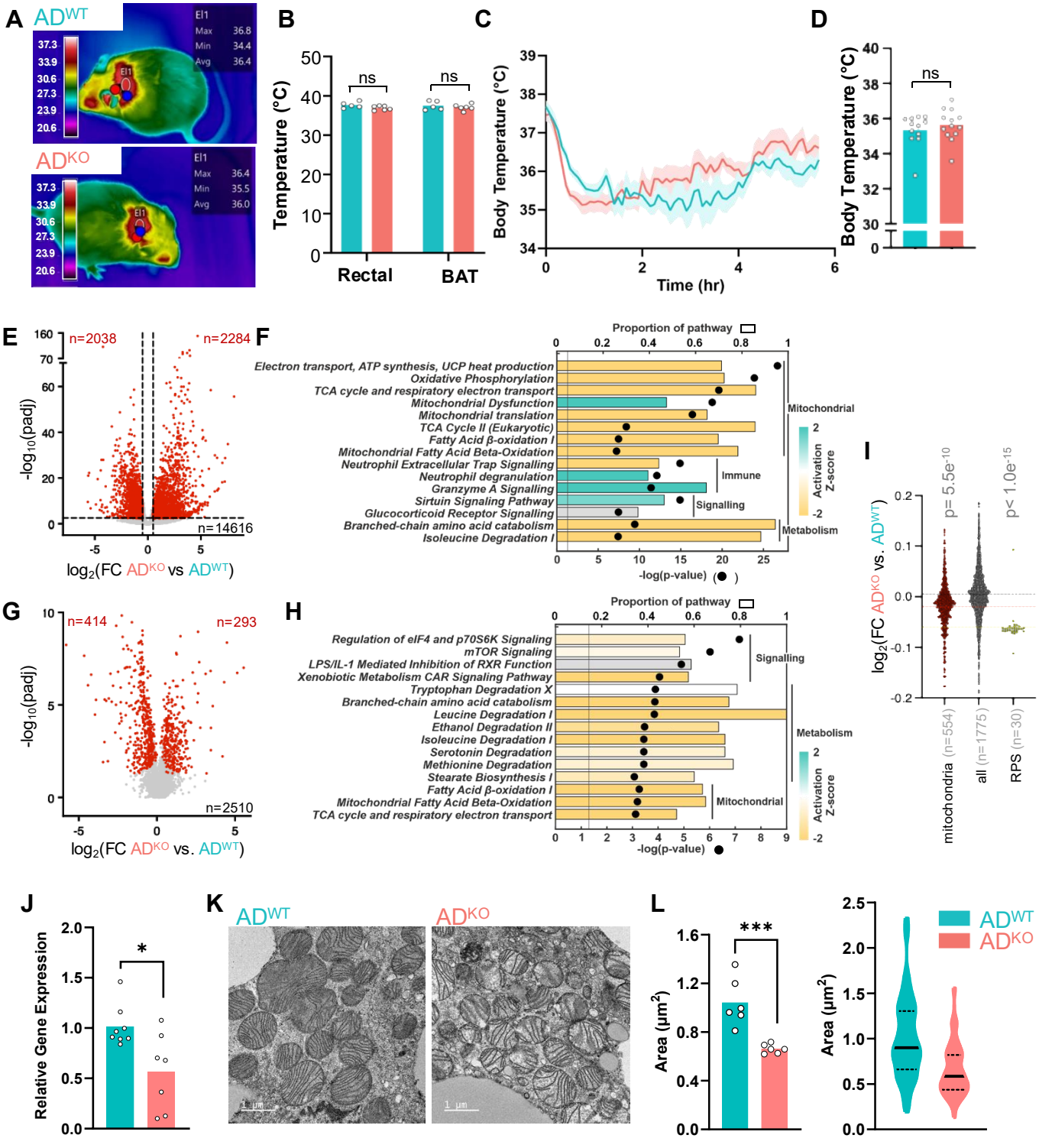

Figure 4. Bud23 directs a selective impact to liver function and proteome

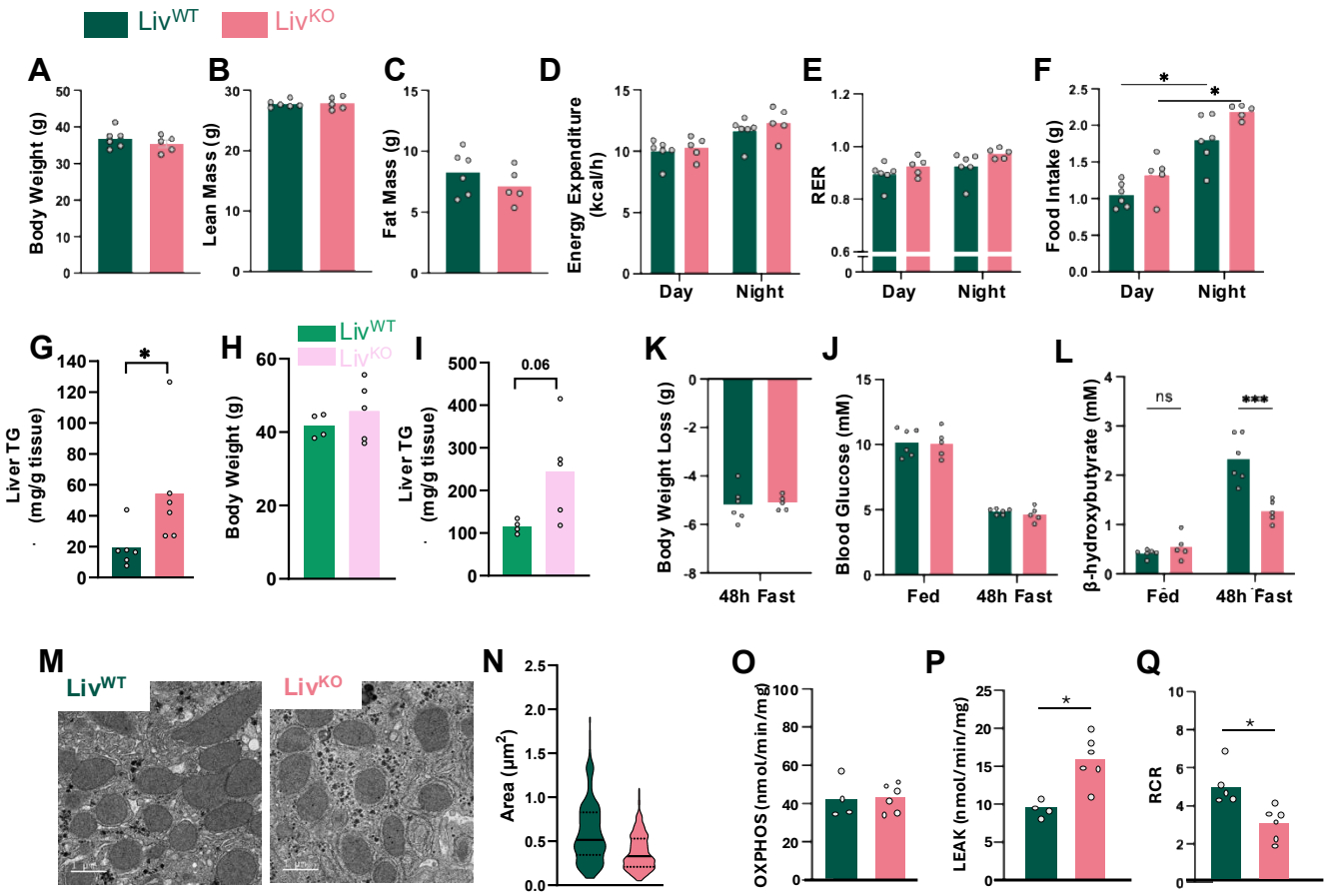

Figure 5. Hepatic Bud23 loss drives selective impact on translation efficiency

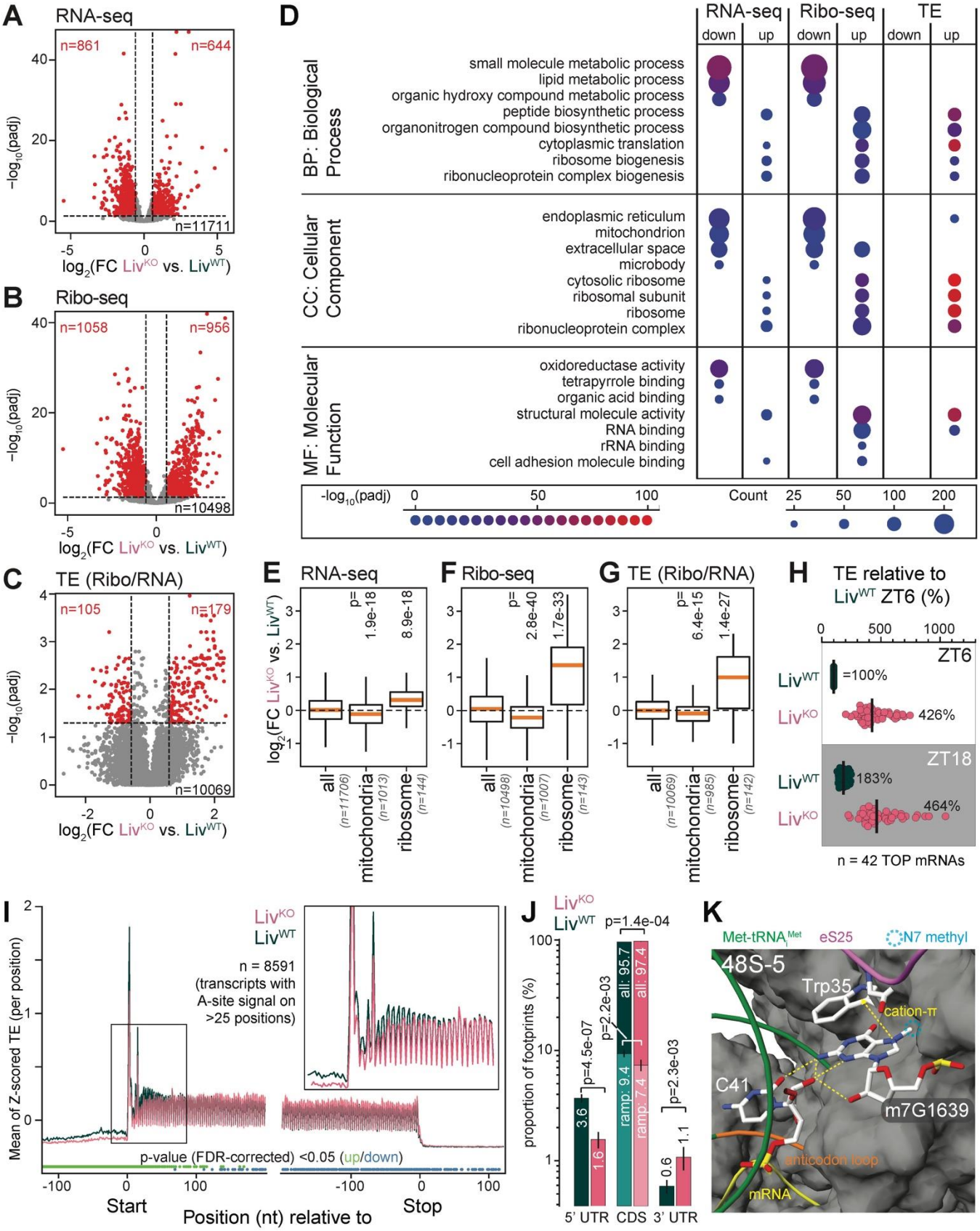

Figure 6. Selective sensitivity of mitochondrial transcripts to Bud23 loss dictated by mRNA features

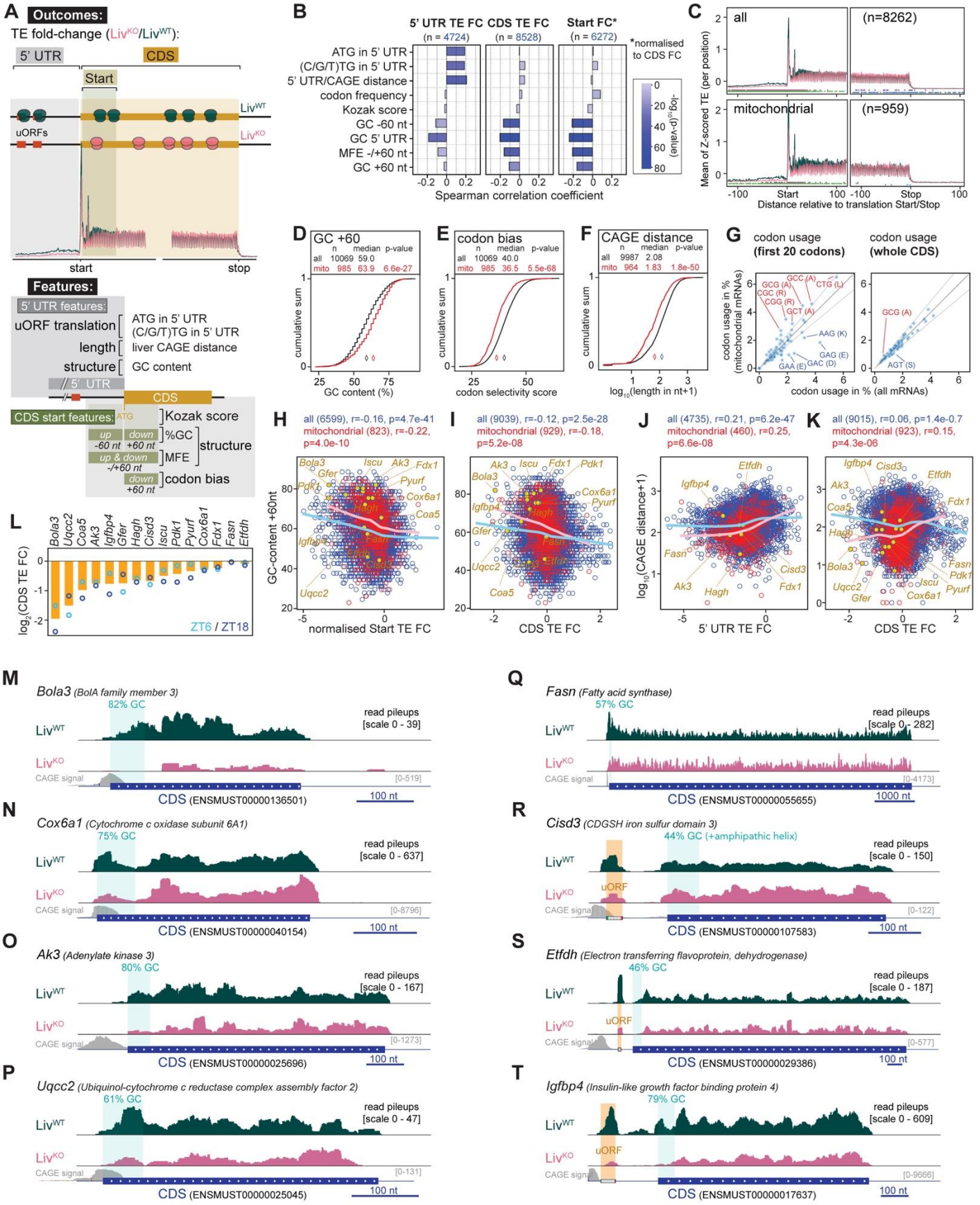

Figure 7. Human genetics

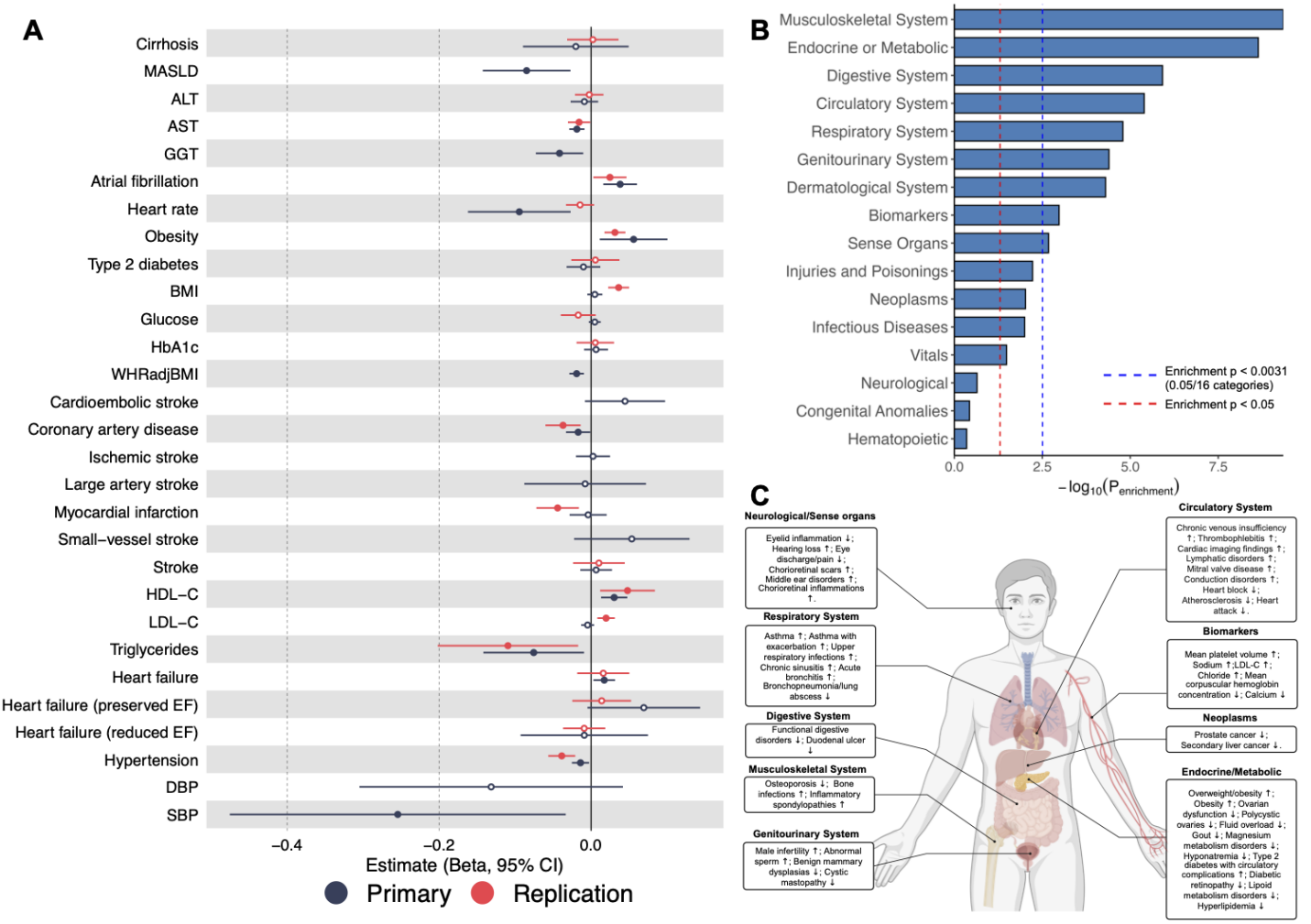

FigureS1. Loss of Bud23 function drives profound metabolic phenotype.

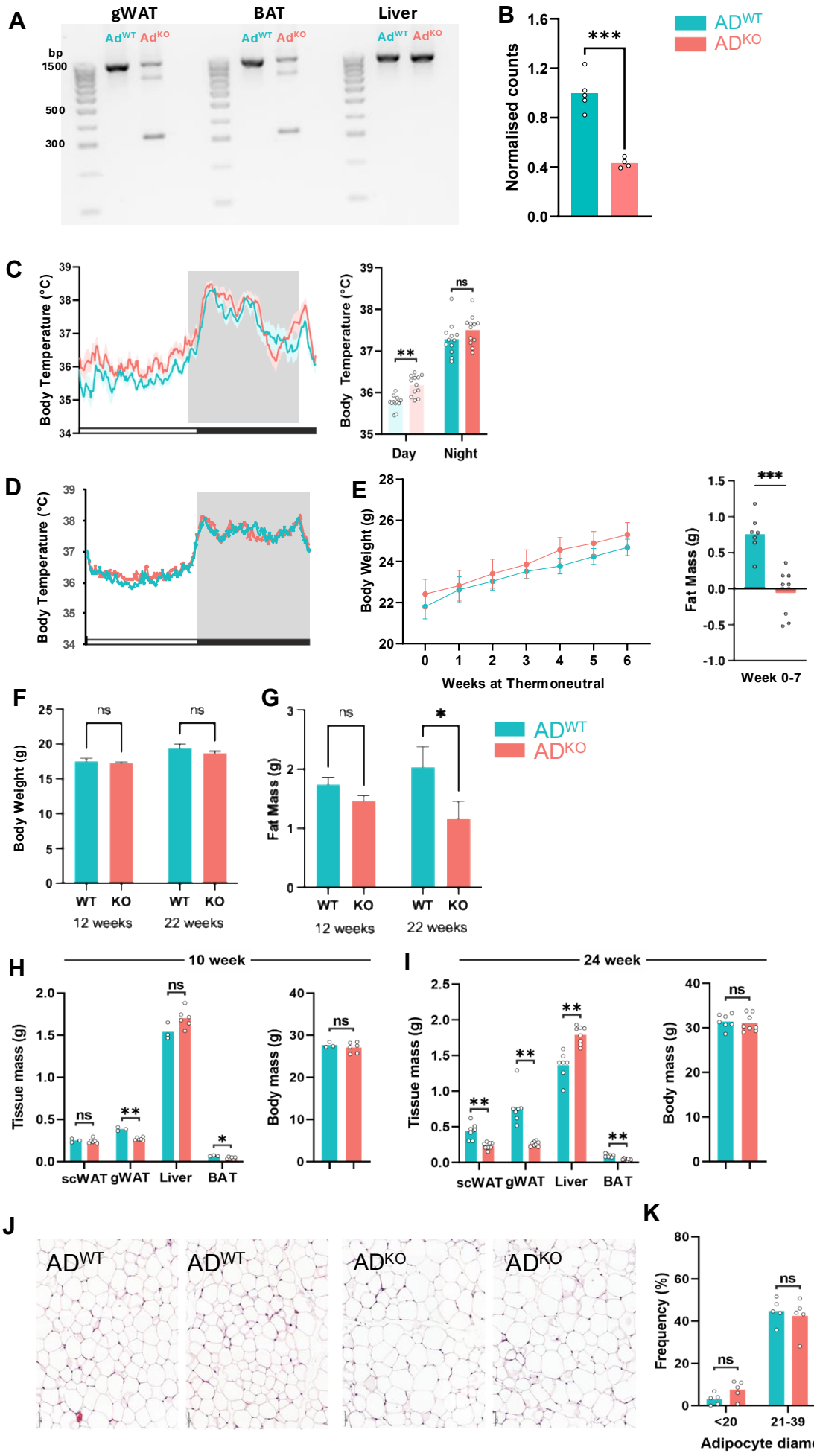

FigureS2. Loss of BUD23 in brown adipocytes drives a mild phenotype

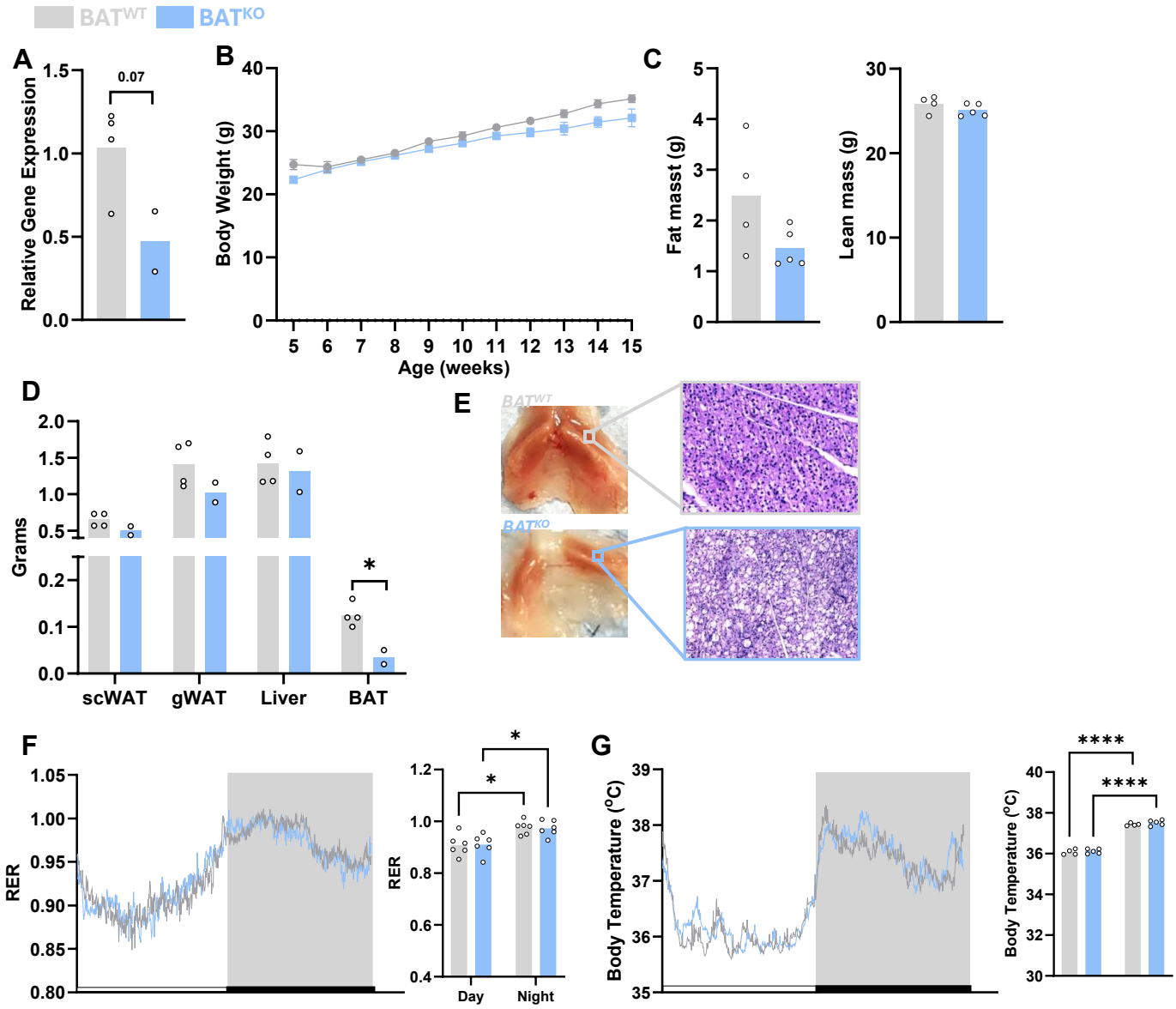

Figure S3. Bud23 is not required for adipocyte differentiation

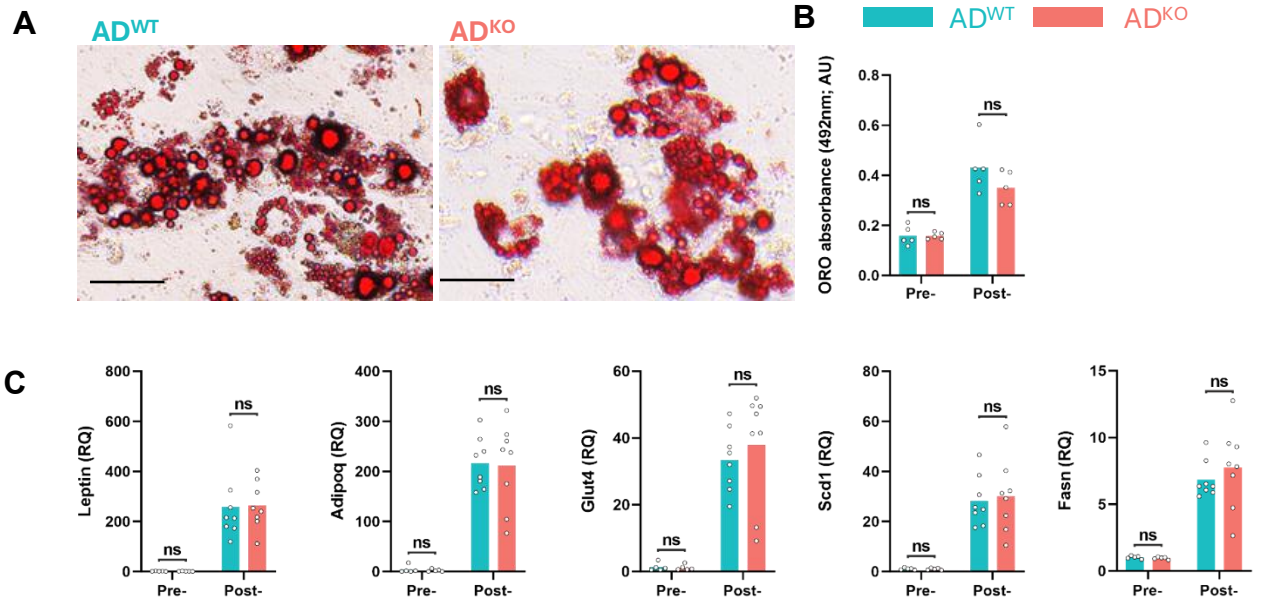

D

UP-REGULATED

GO Process	Gene Count	FDR
RNA processing	193	9.98E-25
Nucleic acid metabolic process	352	9.98E-25
RNA metabolic process	264	8.13E-21
ncRNA metabolic process	132	7.44E-20
Gene expression	327	2.24E-19
ncRNA processing	113	2.87E-19
Nucleobase-containing compound metabolic process	378	1.65E-17
Ribonucleoprotein complex biogenesis	114	6.28E-17
Heterocycle metabolic process	387	4.58E-16
Cellular aromatic compound metabolic process	388	4.75E-15
Organic cyclic compound metabolic process	411	4.75E-15
rRNA metabolic process	77	1.49E-14
Ribosome biogenesis	85	1.60E-13
rRNA processing	70	4.05E-13
Cellular nitrogen compound metabolic process	428	2.29E-12
Defense response to other organism	135	1.75E-07
Innate immune response	109	3.26E-07
RNA modification	45	7.30E-07
Immune response	159	9.82E-07

GO Component		
Nucleus	798	3.54E-16
Nucleolus	178	1.30E-12
Nuclear protein-containing complex	214	1.40E-12
Intracellular organelle lumen	543	3.49E-09
Ribonucleoprotein complex	130	3.49E-09
Preribosome	33	1.34E-08
Nucleoplasm	434	3.25E-07
Intracellular non-membrane-bounded organelle	508	1.19E-06
Protein-containing complex	585	1.84E-05
Spliceosomal complex	46	3.74E-05
U2-type spliceosomal complex	28	0.00021
Small-subunit processome	16	0.00072

Reactome		
Metabolism of RNA	124	6.05E-11
Processing of Capped Intron-Containing Pre-mRNA	60	2.27E-05
Major pathway of rRNA processing in the nucleolus and cytos	43	9.71E-05
Cell Cycle	94	0.00012
Cell Cycle, Mitotic	83	0.00012
mRNA Splicing - Major Pathway	45	0.00012
Innate Immune System	120	0.0022
Mitotic Metaphase and Anaphase	44	0.0022
M Phase	61	0.0022
Cell Cycle Checkpoints	50	0.0022
Mitotic Anaphase	43	0.0033
Mitotic Spindle Checkpoint	27	0.004
snRNP Assembly	16	0.0094
Amplification of signal from unattached kinetochores via a M	23	0.0106
Immune System	180	0.0281

DOWN-REGULATED

GO Process	Gene Count	FDR
Small molecule metabolic process	273	1.99E-18
Generation of precursor metabolites and energy	103	5.35E-16
Monocarboxylic acid metabolic process	122	2.05E-15
Oxoacid metabolic process	161	2.60E-14
Carboxylic acid metabolic process	159	2.86E-14
Organic acid metabolic process	163	4.89E-14
Energy derivation by oxidation of organic compounds	79	5.43E-13
Lipid metabolic process	192	2.09E-11
Aerobic respiration	54	2.00E-10
Cellular lipid metabolic process	156	2.00E-10
Fatty acid metabolic process	83	3.62E-10
Oxidative phosphorylation	45	1.37E-09
Cellular respiration	58	2.44E-09
Carboxylic acid catabolic process	62	3.90E-09
Purine ribonucleotide metabolic process	80	6.13E-08
Organophosphate metabolic process	143	7.89E-08
Ribose phosphate metabolic process	84	8.96E-08
ATP synthesis coupled electron transport	29	2.37E-06
Electron transport chain	38	2.51E-06

GO Component		
Membrane	921	2.11E-20
Inner mitochondrial membrane protein complex	52	1.14E-10
Mitochondrion	279	3.69E-10
Mitochondrial membrane	139	2.58E-09
Mitochondrial envelope	144	7.87E-09
Respiratory chain complex	36	1.04E-08
Oxidoreductase complex	39	2.91E-07
Mitochondrial protein-containing complex	65	8.47E-07
Organelle inner membrane	105	1.52E-06
Cytochrome complex	20	3.96E-06
Organelle envelope	185	4.66E-06
Mitochondrial respiratory chain complex IV	15	2.87E-05
Cytoplasm	1083	0.00019
Endoplasmic reticulum	227	0.00021
Anchoring junction	153	0.00034
Mitochondrial proton-transporting ATP synthase complex	11	0.0017

Reactome		
Metabolism	309	8.13E-24
The citric acid (TCA) cycle and respiratory electron transpor	58	1.94E-11
Respiratory electron transport, ATP synthesis by chemiosmo	40	3.28E-07
Metabolism of lipids	106	3.28E-07
Fatty acid metabolism	42	1.71E-05
Respiratory electron transport	30	9.91E-05
Pyruvate metabolism and Citric Acid (TCA) cycle	18	0.0017
Branched-chain amino acid catabolism	12	0.002
Metabolism of carbohydrates	49	0.0023
Biotin transport and metabolism	9	0.0038
Mitochondrial fatty acid beta-oxidation of saturated fatty ac	8	0.0067

Figure S4. Bud23 directs brown adipose tissue morphology, lipid metabolism and mitochondrial function.

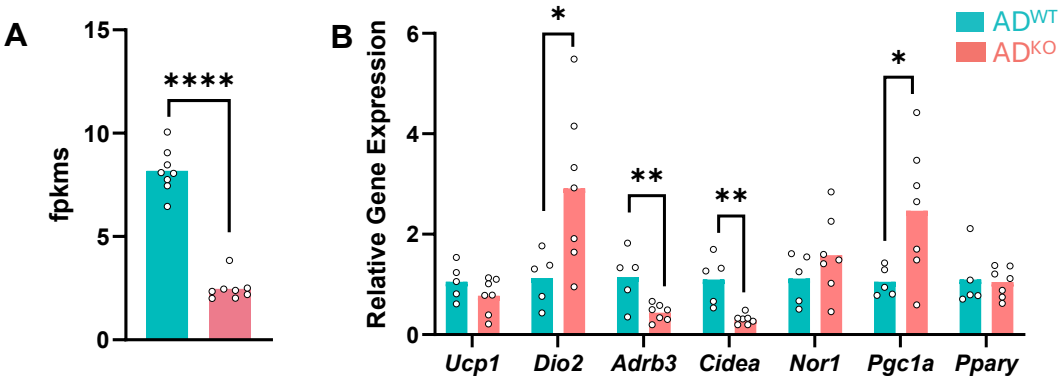

C

DOWNREGULATED

GO_Biological Process	Protein Count	FDR
Fatty acid metabolic process	66	2.58E-08
Carboxylic acid catabolic process	53	1.71E-07
Fatty acid beta-oxidation	27	0.00025
Purine nucleoside bisphosphate metabolic process	28	0.00074
Alpha-amino acid metabolic process	33	0.0038
Ribosomal small subunit biogenesis	16	0.0051
GO_Component		
Cytosolic small ribosomal subunit	30	2.62E-07
Mitochondrial matrix	60	0.0208
Mitochondrial envelope	102	0.0397
Peroxisome	24	0.0397
Reactome		
Metabolism of lipids	66	3.74E-07
Formation of ternary complex and 43S complex	29	2.65E-05
Fatty acid metabolism	38	2.65E-05
Branched-chain amino acid catabolism	15	0.0018
Mitochondrial Fatty Acid Beta-Oxidation	17	0.01

UP

GO_Biological Process	Protein Count	FDR
Immune response	40	0.0372

D

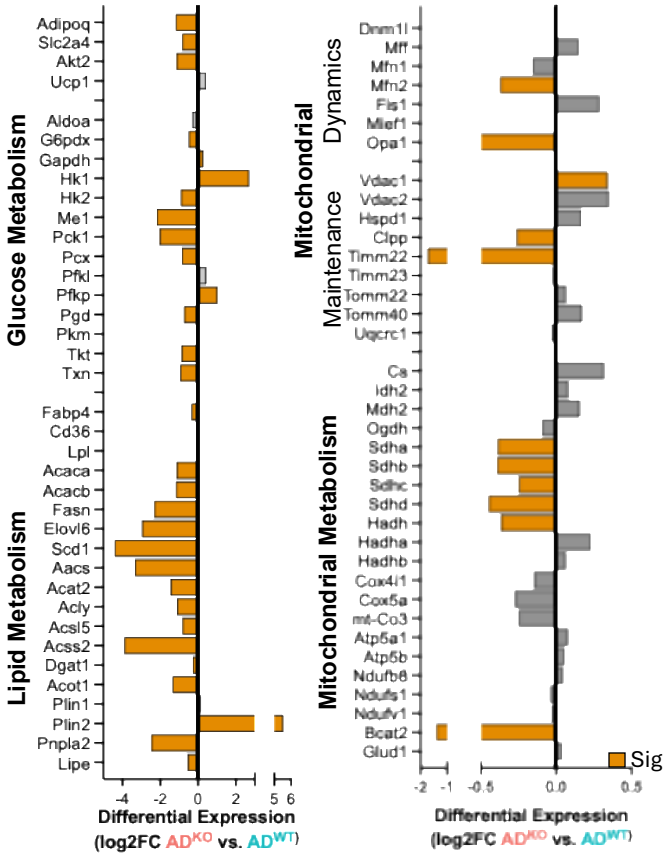

FigureS5. Bud23 targeting in Liver

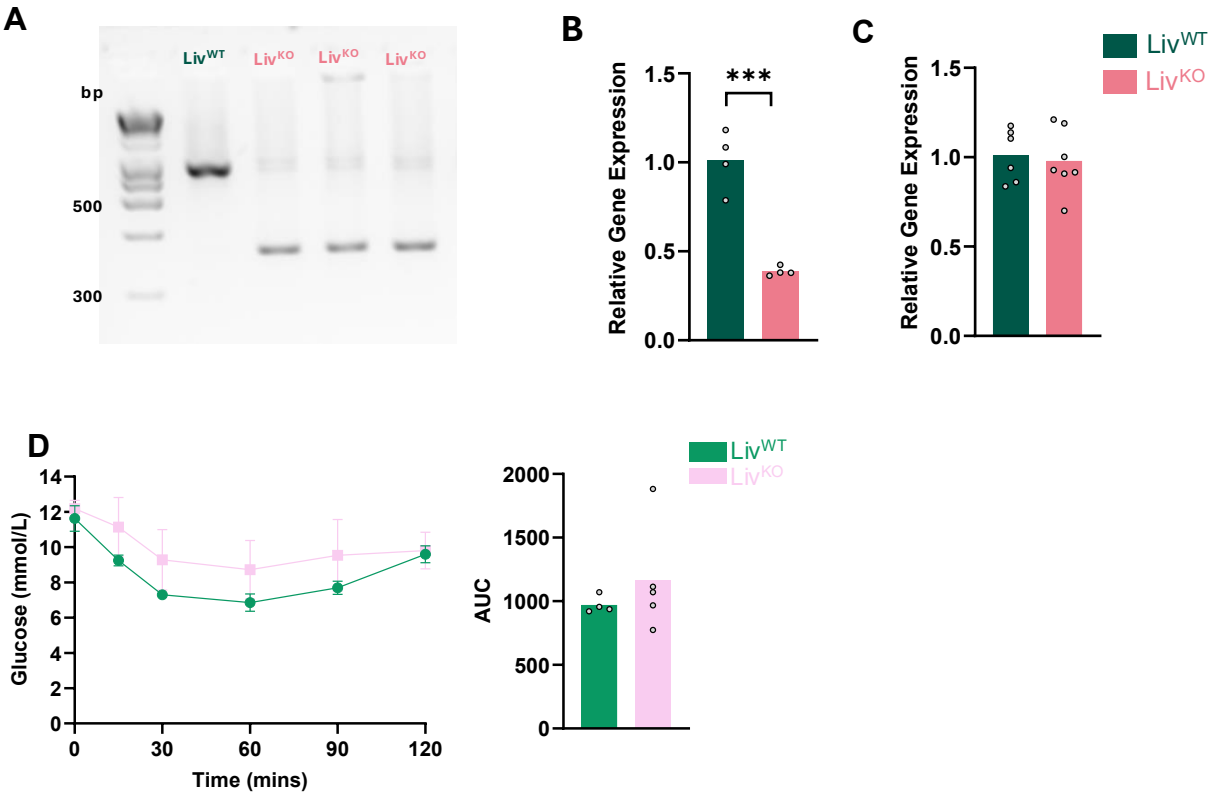

FigureS6. Extended Figure 5a

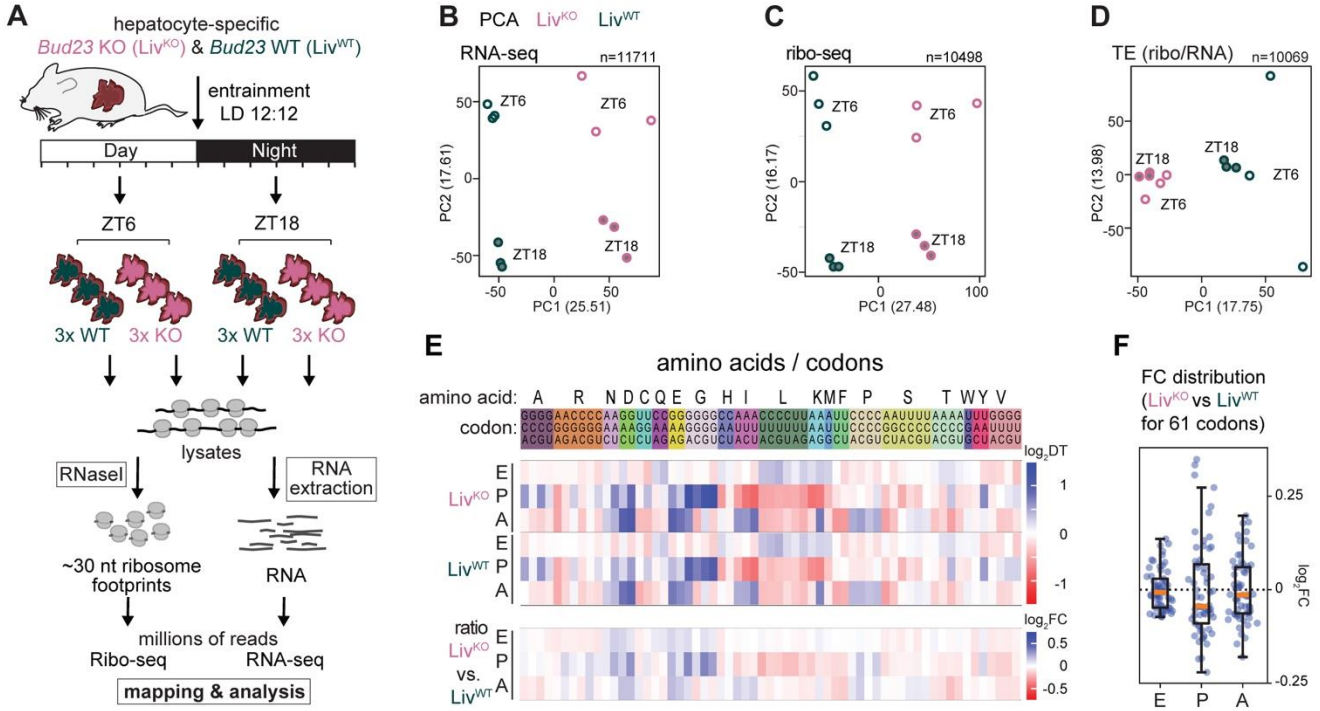

FigureS7. Extended Figure 5b

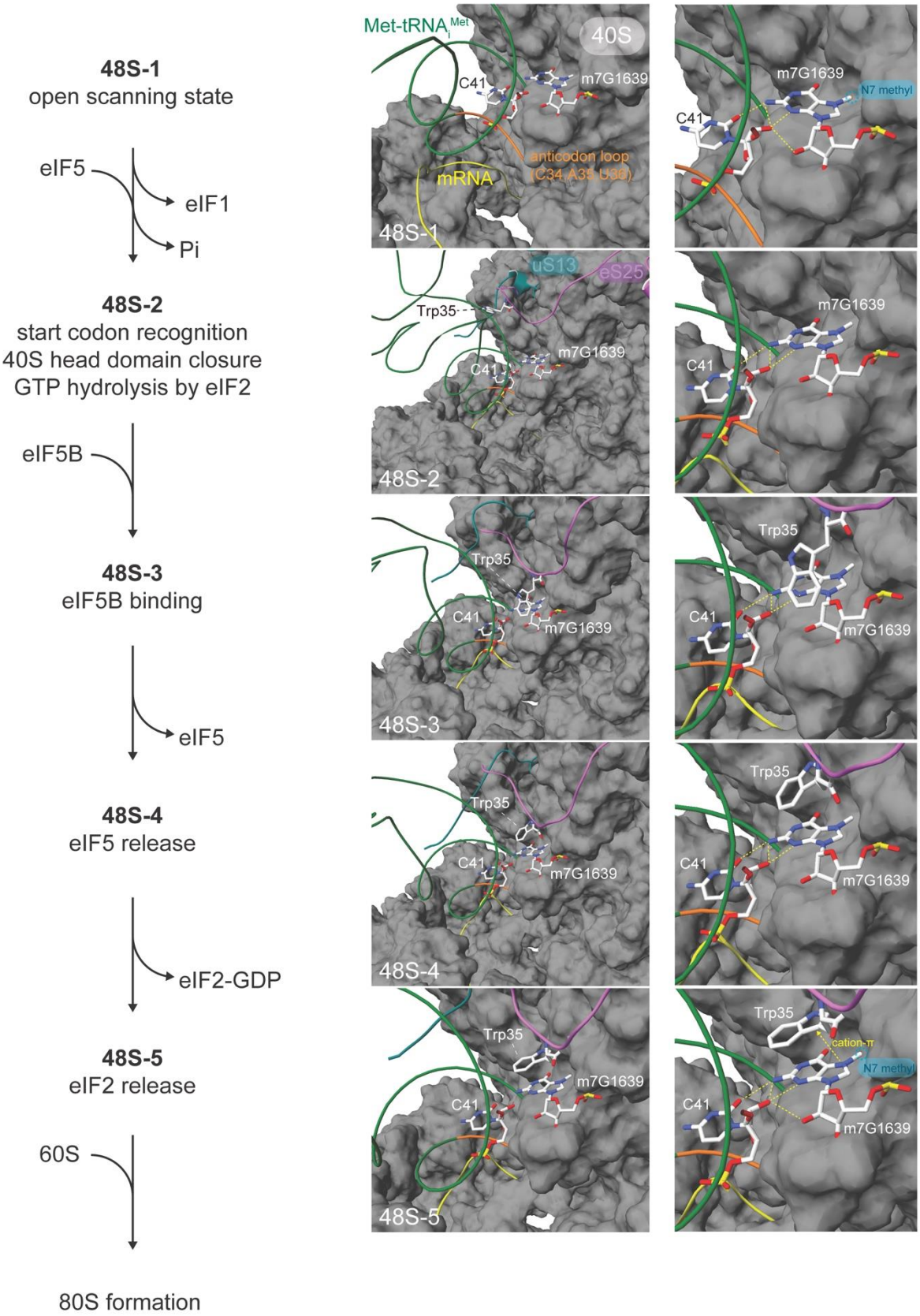

FigureS8. Extended Figure 6

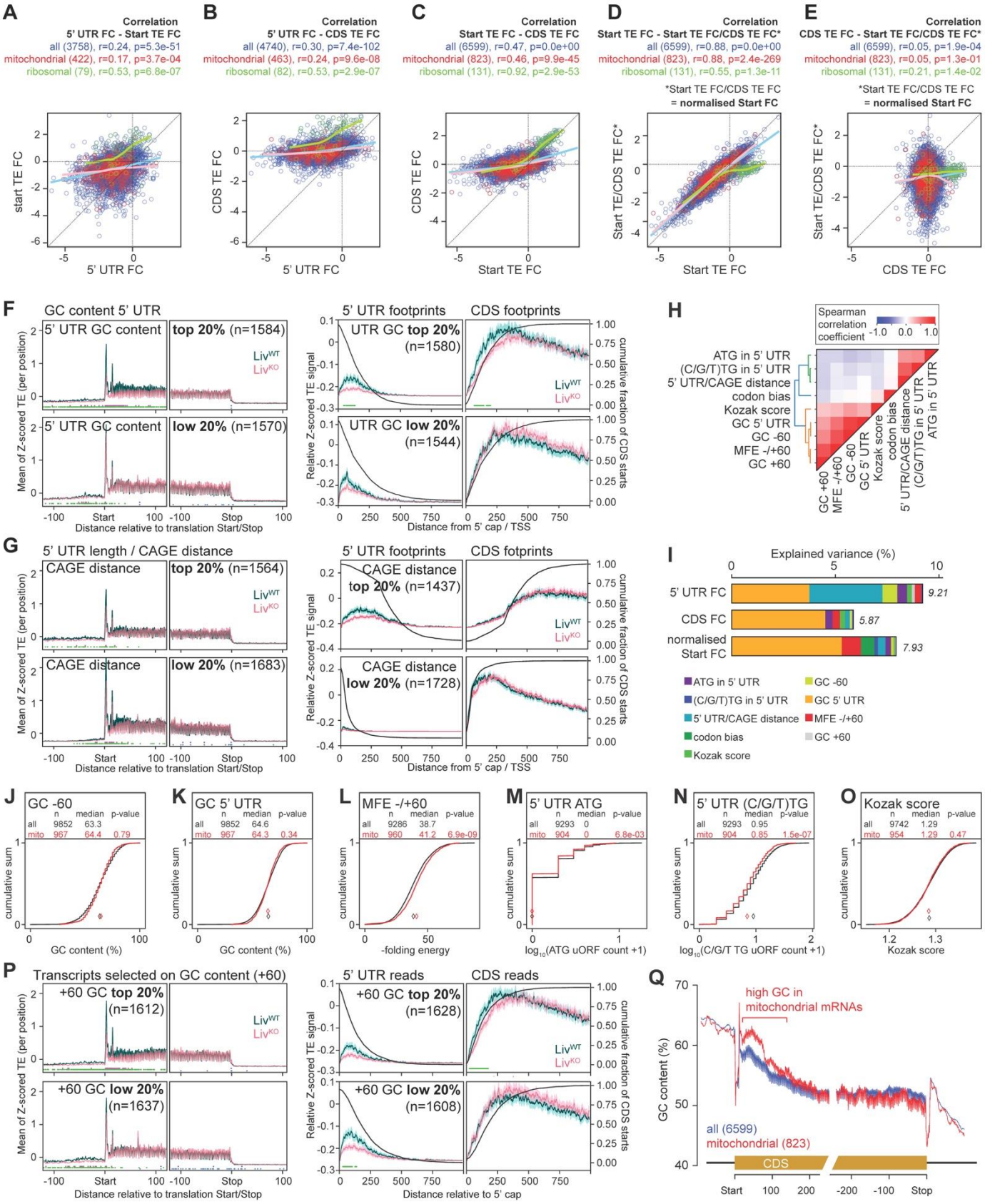

FigureS9. Human genetics

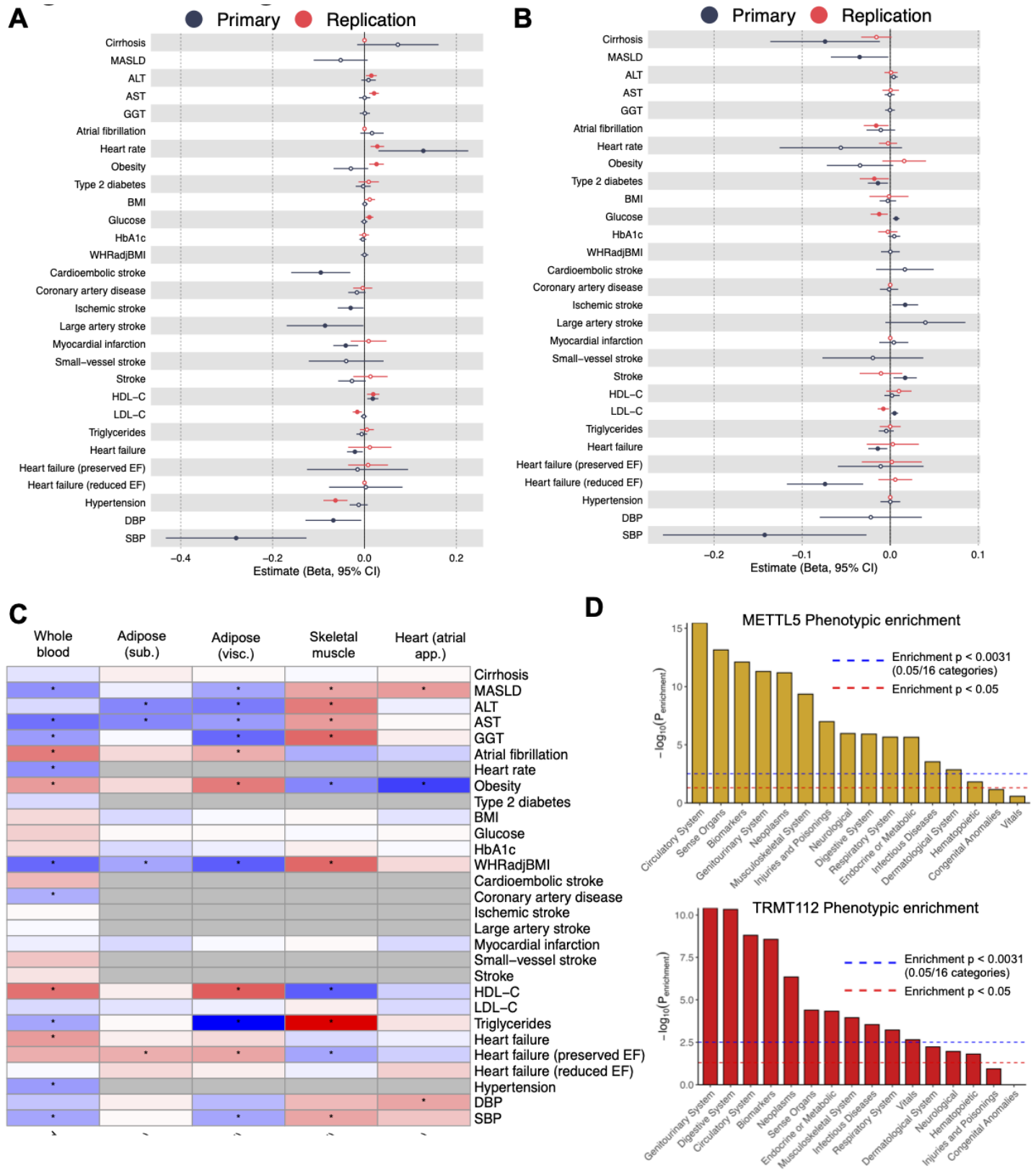

Figure Legends

Figure 1. Loss of Bud23 function drives profound metabolic phenotype and shift in body composition.

(**A**) Body weight change of Bud23$^{fl/fl}$ Adipoq^{Cre+} (AD^{KO} n=9) mice compared to littermate controls, Bud23$^{fl/fl}$ (AD^{WT}, n= 11). (**B**) Body composition of AD^{KO} and AD^{WT}, with total fat mass (left and middle panels) and lean mass (right panel). Histograms reflect body composition at 24 wks. (**C**, **D**) Food intake (**C**) and faecal energy content (**D**) of AD^{WT} and AD^{KO} mice (food intake, n=6 per group; faecal energy content, n=5-7 mice/group). (**E-H**) Locomotor activity (**E**), Energy Expenditure (**F**) and Respiratory Exchange Ratio (RER) (**G,H**) in AD^{WT} and AD^{KO} mice (n=6 mice/group). (**I**) Representative picture and histology of the gonadal white adipose tissue (gWAT) of AD^{WT} and AD^{KO} mice. (**J**, **K**) Circulating serum lipids (triglyceride, NEFA and glycerol) and adipokines (leptin, adiponectin and resisting) in AD^{WT} and AD^{KO} mice (n= 5-7 mice/group). (**L**) Representative picture and histology of Brown Adipose Tissue (BAT) of AD^{WT} and AD^{KO} mice mice. (**M**, **N**) Liver weight and triglyceride content of AD^{WT} and AD^{KO} mice (males, n=6-8 mice/group). (**O**, **P**) Percentage of lipogenesis de novo in liver and Brown Adipose Tissue (BAT) in AD^{WT} and AD^{KO} mice (n=5 mice/group) (O=% newly synthesised 16:00 from ^{13}C glucose; P= % newly synthesised 16:00). (**Q**) Body weight of AD^{KO} and AD^{WT} during 9 wks of high fat diet (HFD) feeding. (**R**) Fat and lean mass of male AD^{KO} and AD^{WT} on high fat diet (HFD). (**S**) Fat mass of female AD^{KO} and AD^{WT} mice on high fat diet (HFD).

Figure 2. Bud23 is required for normal white adipocyte function.

(**A**) Volcano plot of differentially expressed genes from RNA sequencing in AD^{KO} gonadal White Adipose Tissue (gWAT) relative to control. Significantly up- (right) and down- (left) regulated transcripts are indicated in red (n=4-5 mice/group). (**B**) Virtual cytometry plot displaying the different cell types from RNA sequencing data in gWAT from AD^{WT} and AD^{KO} mice (n=4-5 mice/group). (**C**) Percentage of lipid-scavenging adipocytes, stressed lipid-scavenging adipocytes and lipogenic adipocytes from gonadal White Adipose Tissue RNA sequencing data in AD^{WT} and AD^{KO} mice (n=4-5 mice/group). (**D**) Gene ontology enrichment of major pathways affected by Bud23 deletion in gWAT. adipocytes (columns represents proportion of pathway, black dot represents p value). (**E**) Specific gene expression changes of genes related to Adipocyte function, Lipid metabolism and Mitochondrial function shown as Log2 fold change (FC), in gWAT. (**F**) Western blot representative images and quantification of ATGL, DGAT2, FAS, LPL in gonadal White Adipose Tissue from AD^{WT} or AD^{KO} mice (n=4-5 mice/group). (**G**) Relative gene expression of adipogenic genes in isolated mature adipocytes (from gWAT) from AD^{WT} control or AD^{KO} mice (*n* = 3 mice/group). (**H**) Intraperitoneal insulin tolerance test (G) and Area Under the Curve (AUC) of AD^{WT} mice and AD^{KO} (*n* = 6 for control group; *n* = 6 for knock-out group). (**I**) Relative gene expression of adipogenic genes in gonadal White Adipose Tissue Explants from AD^{WT} control or AD^{KO} mice treated with Insulin or vehicle (*n* = 3-6 mice/group).

Figure 3. Bud23 directs brown adipose tissue morphology, lipid metabolism and mitochondrial function.

(**A, B**) Representative Infrared thermal images of Brown Adipose Tissue (BAT) skin area and rectal and BAT temperature of AD^{WT} and AD^{KO} mice (n=5-6 mice/group). (**C, D**) Body Temperature of AD^{WT} and AD^{KO} mice exposed to 4°C during 6 hours. (**E**) Volcano plot of differentially expressed genes from RNA sequencing in AD^{KO} Brown Adipose Tissue (BAT) relative to AD^{WT} BAT. (*n* = 8 mice/group). (**F**) Gene ontology enrichment of major pathways

affected by Bud23 deletion in adipocytes (columns represent proportion of pathway, dots represent p value). (**G**) Volcano plot of total proteins from Proteomoics analysis in AD^{KO} BAT relative to AD^{WT} BAT. (n= 7-8 mice/group). (**H**) Gene ontology analysis of major protein pathways affected by Bud23 deletion in adipocytes (columns represent proportion of pathway, dots represent p value). (**I**) Genotype-specific differences in global protein abundance (RPS= small subunit ribosome). (**J**) BAT mitochondria copy number of AD^{WT} and AD^{KO} mice. (**K-L**) Representative electron microscopy images (**K**), mitochondrial area quantification (average per mouse) (**L**, left panel), and area of all mitochondria analysed (**L**, right panel) of BAT slices from AD^{WT} and AD^{KO}.

Figure 4. Bud23 directs a selective impact to liver function and proteome.

(**A-C**) Body weight, lean mass and fat mass at terminal point of $Bud23^{fl/fl}$ $AlbCre^{Cre+}$ mice (Bud23 knock-out targeted to hepatocytes (Liv^{KO}), compared to littermate controls, $Bud23^{fl/fl}$ (Liv^{WT}) (n=5-6 mice group). (**D-F**) Energy expenditure, respiratory exchange ratio (RER) and food intake of Liv^{KO}, compared to littermate controls, Liv^{WT} (n=5-6 mice/group). (**G**) Hepatic triglycerides levels of Liv^{KO} mice and their littermate controls, Liv^{WT} (n=6 mice/group). (**H, I**) Body weight and hepatic triglycerides leves of Liv^{KO} mice and their littermate controls on High Fat Diet (HFD). (**K-L**) Body weight loss, blood glucose and β-hydroxybutirate levels of Liv^{KO} mice and their littermate controls, at feeding state and after 48 hours fasting. (**M**, **N**) Representative electron microscopy images (**M**) and area of all mitochondria analysed (**N**) of liver tissue slices from Liv^{WT} and Liv^{KO}. (**O-Q**) OROBOROS mitochondrial respiration analysis of isolated mitochondria from liver of Liv^{KO} and their control littermates

Figure 5. Hepatic *Bud23* drives selective impact on translation efficiency.

(**A**) Volcano plot of differentially expressed genes in liver from RNA sequencing in Liv^{KO} vs. Liv^{WT}. Significantly up- (right) and down- (left) regulated transcripts with adjusted p value <0.05 and absolute log2 fold change >1.5 are indicated in red. All 6 samples, irrespective of the Zeitgeber time points (3 for ZT6 and 3 for ZT18), were compared between genotypes. (**B**) Volcano plot as in (**A**) but for Ribo-seq data. (**C**) Volcano plot as in (A) and (B) but for translation efficiencies (TE, ratio of normalised Ribo-seq to RNA-seq reads calculated per liver sample). (**D**) GO-term analysis on differentially expressed gene sets shown in (A) - (C). Most significant enrichments are shown. Size of circles indicates the number of genes within a category; colour coding indicates statistical significance, as illustrated in the legend in lower part of panel. (**E**) Boxplot representation of log_2 fold-changes between Liv^{KO} vs. Liv^{WT} for all transcripts, mitochondrial transcripts (annotation from MitoCarta3.0), and ribosomal transcripts (from GO cellular component). Log2 fold changes were calculated between all 6 samples of each genotype. Boxes cover the interquartile range, with whisters extending to 1.5x interquartile range; median marked in red. p-values indicate significance assessed by a ranksum test. (**F**) Boxplot representation as in (**E**) for Ribo-seq data. (**G**) Boxplot representation as in (E) for translation effficiency. (**H**) Translation efficiency in Liv^{KO} (pink) and Liv^{WT} (dark green) at ZT6 (light phase) and ZT18 (dark phase) of selected ribosomal protein/translation factor mRNAs (n=42) that contain a 5'-TOP sequence and that were previously identified as particularly rhythmic in their TE [24]. For each transcript, TE is expressed relative to the level in Liv^{WT} at ZT6, which was set to 100%. (**I**) Metagene plot aligning ribosome footprint A-sites relative to coding sequence (CDS) start (left) and stop (right) codons, for Liv^{KO}

(pink) and Liv^{WT} (dark green). Transcripts are included with A sites at 25 or more positions within the shown range of nucleotides (n=8591). Dots below the plot indicate positions with a ratio between A sites for Liv^{KO} and Liv^{WT} significantly higher (green) or lower (blue) than 0 calculated using a directional one-sample t test. The inset at the top right shows a zoom on the area around the start codon, indicating a specific decrease of ribosomes in Liv^{KO} over the first ~20 codons and the 5' UTR. (**J**) Quantification of global read distribution in Liv^{KO} (pink) and Liv^{WT} (dark green) for 5' UTR, CDS (all and first 20 codons in light colors) and 3' UTR. Error bars indicate the standard deviation across the 6 samples per genotype. P-values indicate statistical significance assessed by a two-tailed independent *t*-test. (**K**) Structural model of human late initiation complex 48S-5 (PDB 8pj5) at the site of m^7G1639. Highlighted residues apart from m^7G1639 (with N7 methyl group marked by blue halo) are Met-$tRNA_i^{Met}$ (backbone traced in green; anticodon loop in orange), tRNA residue C41 that forms extensive hydrogen bonds with m^7G1639. Trp35 of eS25/RPS25 is placed for cation-π stacking onto m^7G1639. mRNA trace is marked in yellow and 18S rRNA surface in grey.

Figure 6. Selective BUD23 regulation is associated with specific transcript features.

(**A**) Schematic of analysis of correlation between transcript features and BUD23-selective regulation. Three "Outcomes", shown at the top of figure, were extracted from the ribo-seq profiles and quantified transcriptome-wide – translation efficiency (TE) change on the 5' UTR (indicative of uORF translation), TE change on the whole CDS (i.e. change in overall translation rate) and specifically within the first 20 codons (the "ramp effect"). These were correlated with "Features" of transcripts, pertaining to the 5' UTR – presence of ATG, (C/G/T) TG, UTR length as determined from cap analysis of gene expression (CAGE) data, GC content – or the CDS initiation codon environment – KOZAK score, GC content, minimal free energy of folding (MFE), codon bias. (**B**) Spearman correlation coefficients between transcript sequence features (y-axis) and translation efficiency log2 fold-changes (beween Liv^{KO} and Liv^{WT}) at 5' UTRs (first panel), CDSs (second panel), and the Start codon region (first 20 codons) relative to the whole CDS (third panel). TE fold changes were calculated as the average over the separate TE fold changes for the two Zeitgeber time points (ZT6 and ZT18). Bars are coloured according to correlation p-value. (**C**) Metagene plot aligning ribosome footprint A-sites relative to coding sequence (CDS) around start (left panels) and stop (right panels) codons, for Liv^{KO} (pink) and Liv^{WT} (dark green) for all transcripts (upper panels) and transcripts encoding mitochondrial proteins (based on MitoCarta 3.0; lower panels). See Fig. 2I for additional information. (**D**) Analysis of GC content within the 60 nt after the start codon, for transcripts encoding mitochondrial proteins (red) vs. all transcripts (black), indicating significantly increased GC-content in the mitochondrial group. In the upper part of the panel, the number of transcripts used for the analysis (n), their median (also shown as diamond symbol in graph) and the p-value for the difference using a ranksum test are given. (**E**) As in (**D**), for codon bias/selectivity for the first 20 codons. Mitochondrial groupis composed of significantly less abundant codons. (**F**) As in (E), for 5' UTR length as determined from cap analysis of gene expression (CAGE) data. Mitochondrial protein mRNAs are characterised by significantly shorter 5' UTRs. (**G**) Analysis of codon composition of first 20 codons (left panel) and whole CDS (right panel), comparing all mRNAs (x-axis) with mitochondrial protein mRNAs (y-axis). Codons are labelled with a 20% higher (red) or lower (blue) abundance in mitochondrial protein mRNAs that in all mRNAs. More abundant codons correspond largely to GC-rich codons associated with amphiphilic helices of mitochondrial targeting signals

enriched in the first 20 codons of mitochondrial protein mRNAs. (**H**) Scatter plot of translation efficiency log2 fold-changes at the first 20 codons relative to whole CDS, beween Liv^{KO} and Liv^{WT}, and GC-content in the same +60 nt region of the transcript. All transcripts and mitochondrial protein mRNAs are shown as blue and red circles, respectively. The local regression fits (LOESS) for all and mitochondrial transcripts are shown in pale blue and pink, respectively. Spearman correlation coefficient and p-value of correlation are given above, alongside number of transcripts used in the analysis. Specific genes/transcripts are highlighted in ochre. (**I**) As in (H), but showing correlation between whole CDS translation efficiency fold-change (Liv^{KO} vs. Liv^{WT})and GC-content of +60 nt region. (**J**) As in (H), but showing correlation between 5' UTRs translation efficiency fold-change (Liv^{KO} vs. Liv^{WT}) and 5' UTR length/CAGE distance. (**K**) As in (H), but showing correlation between CDS fold-change (Liv^{KO} vs. Liv^{WT}) and 5' UTR length/CAGE distance. (**L**) Quantification of CDS translation efficiency change (Liv^{KO} vs. Liv^{WT}) for selected transcripts labelled in panels (H) - (K). Values for ZT6 and ZT18 are plotted individually as circles, with orange bars showing the mean. (**M**) Genome browser tracks showing read pile-up along *Bola3 (BolA familiy member 3)* transcript in Liv^{WT} (upper track, dark green) and Liv^{KO} (lower track, pink). Grey track shows CAGE signal from mouse liver FANTOM5 data (i.e. this 5' UTR is extremely short). Transcript model and scale bar shown in blue. Green shading placed on first 20 codons, with GC content written above (82%). Data from ZT18 are plotted, combining reads from the three biological replicates. (**N**) As in (M) for *Cox6a1 (Cytochrome c oxidase subunit 6A1)*. This transcript has very high GC content and very short 5' UTR. (**O**) As in (M) for *Ak3 (Adenylate kinase 3)*. This transcript has very high GC content and relatively short 5' UTR. (**P**) As in (M) for *Uqcc2 (Ubiquinol-cytochrome c reductase complex assembly factor 2)*. This transcript has average GC content yet very short 5' UTR. (**Q**) As in (M) for *Fasn (Fatty Acid synthase)*. *Fasn* has average GC and a relatively short 5' UTR. (**R**) As in (M) for *Cisd3 (CDGSH iron sulfur domain 3)*. Theposition of a uORF is indicated by orange shading. (**S**) As in (R) for *Etfdh (Electron transferring flavoprotein, dehydrogenase)*. (**T**) As in (R) for *Igfbp4 (Insulin-like growth factor binding protein 4).*

Figure 7. Human Genetic Evidence Linking Whole Blood BUD23 Expression to Cardiometabolic Disease Outcomes.

This figure presents Mendelian Randomization (MR) analyses modeling the effect of genetically increased BUD23 expression in whole blood on human disease and biomarker traits. (**A**) Forest plots display MR estimates (Beta ± 95% CI) across cardiometabolic outcomes in both primary and replication GWAS datasets. Estimates reflect the direction and magnitude of association per unit increase in genetically predicted BUD23 expression. (**B**) Enrichment analysis summarizing phenome-wide MR associations across ~1,200 traits in the Million Veteran Program (MVP), grouped by clinical domain. Bar heights represent enrichment significance, indicating domains with disproportionate representation of associated traits. (**C**) Homunculus schematic mapping representative traits that surpassed FDR correction (FDR < 0.05) within each disease category. Arrows denote the direction of association per increased BUD23 expression: upward arrows indicate positive associations with the outcome, while downward arrows indicate negative associations.

<u>Supplementary Figure Legends</u>

Figure S1. Loss of Bud23 function drives profound metabolic phenotype.

(**A**) Representative agarose gel image of the recombination to ensure knockdown in gonadal White Adipose Tissue (gWAT) and Brown Adipose Tissue (BAT) (liver was included as a negative control). Band at approximately 350bp in gWAT and BAT of AD^{KO} animals indicated recombination. (**B**) Bud23 expression from RNAseq normalised counts gonadal White Adipose Tissue (gWAT) from AD^{WT} or AD^{KO}. (**C**) Body temperature over 24 hours and total day/night of AD^{WT} or AD^{KO}. (**D, E**) Body temperature, body weight change and fat mass of AD^{WT} or AD^{KO} at thermoneutrality (28°C). (**F**, **G**) Body weight and total fat mass of female AD^{WT} or AD^{KO} at age 12 weeks and 24 weeks. (**H, I**) Tissue mass and body mass of male AD^{KO} mice and their littermate controls ^{fl} at 10 weeks old and 24 weeks old. (**J, K**) H&E representative images and Percentage of different Adipocyte diameter (um) in gonadal White Adipose Tissue (gWAT) of AD^{KO} .

Figure S2. Loss of BUD23 in brown adipocytes drives a mild phenotype.

(**A**) Relative Bud23 expression in BAT of BAT^{WT} and BAT^{KO} mice. (**B, C**) Body weight change and fat and lean mass of BAT^{KO}, compared to littermate controls BAT^{WT}. (**D**) Fat depots mass of BAT^{WT} and BAT^{KO} mice. (**E**) Representative picture and histology of the Brown Adipose Tissue (BAT) of BAT^{KO} and BAT^{WT}. (**F, G**) Respiratory Exchange Ratio (RER) and body temperature over 24 hours and at day/night of BAT^{KO} and BAT^{WT}.

Figure S3. Bud23 is not required for adipocyte differentiation.

(**A, B**) Representative pictures of Oil Red O (ORO) staining (A) and quantification (B) in differentiated gWAT adipocytes from AD^{WT} and AD^{KO} mice. (**C**) Relative mRNA expression levels of endocrine hormones, lipolitic and lipogenic genes in gonadal White Adipocytes (gWAT) pre-adipocytes from AD^{WT} and AD^{KO} mice, before and after differentiation (each dot represents a biological replicate). (**D**) Gene Ontology (GO) terms for Biological Process, Cellular Component and Reactome are shown, with directionality indicated as downregulated or upregulated, the number of proteins associated with each GO term and the corresponding false discovery rate (FDR) values.

Figure S4. Bud23 directs brown adipose tissue morphology, lipid metabolism and mitochondrial function

(**A**) Bud23 expression from RNAseq in BAT of AD^{WT} and AD^{KO} mice. (**B**) Relative mRNA expression levels of themogenic genes in BAT from AD^{WT} and AD^{KO} mice. (**C**) Gene Ontology (GO) terms for Biological Process, Cellular Component and Reactome are shown, with directionality indicated as downregulated or upregulated, the number of proteins associated with each GO term and the corresponding false discovery rate (FDR) values, in BAT in AD^{KO} mice. (**D**) Specific gene expression changes of genes related to glucose and lipid metabolism (left panel) and Mitochondrial function and metabolism (right panel) shown as Log2 fold change (FC), in BAT in AD^{KO} mice

Figure S5. Bud23 targeting in Liver.

(**A, B**) Representative agarose gel image of the recombination to ensure knockdown and relative Bud23 epression in liver of LIV^{WT} and LIV^{KO}. (**C**) Mitochondria copy number of liver in liver of LIV^{WT} and LIV^{KO} mice. (**D**) Glucose levels during Insulin Tolerance Test and Area Under the Curve (AUC) LIV^{WT} and LIV^{KO} mice on High Fat Diet (HFD).

Figure S6. Extended Figure 5A.

(**A**) Schematic showing the design of the ribosome profiling experiment. (**B**) Principal component analysis on the RNA-seq data, showing separation on PC1 by genotype – Liv^{KO} (pink) vs. Liv^{WT} (dark green) – and by timepoint on PC2. (**C**) As in (B) for the ribosome footprint data. (**D**) As in (B) for translation efficiencies (i.e., ratio of normalized ribo-seq to RNA-seq reads per gene). In this analysis, main separation occurs by genotype (PC1) with little influence by ZT. (**E**) Analysis of dwell times of elongating ribosomes using the RiboDT pipeline [29]. Upper two sets show heat-maps of dwell times for E- P- and A-sites in Liv^{KO} and Liv^{WT} data (ZT6 and ZT18 combined data) and indicate very similar preference for codon occupancies between genotypes. Lower part shows fold-change differences in dwell times, Liv^{KO} vs. Liv^{WT}, again indicating relatively mild differences in codon-specific dwelling between genotypes. (**F**) Box plots of dwell time log2 fold changes between genotypes (same as lower panel of (E)) at E-, P- and A-sites indicate that overall codon-specific variation appears more prominent at the P-site as compared to E- or A-sites.

Figure S7. Extended Figure 5B.

Overview of structural models of human early (48S-1) to late initiation complexes (48S-5) emphasizing m^7G1639 surroundings (based on PDB structures 8pj1-5). Left part of the Figure illustrates the sequence of 48S state transitions to 80S formation with major rearrangements between them. Middle panels are zoom-out, and right panels zoom-in views of the structural models. Important highlighted residues apart from m^7G1639 (with N7 methyl group marked by blue halo in some of the panels) are Met-$tRNA_i^{Met}$ (backbone traced in dark green; anticodon loop in orange), tRNA residue C41 that forms extensive hydrogen bonds with m^7G1639; eS25/RPS25 (backbone traced in purple) Trp35 is progressively brought close to m^7G1639 up to a point where it makes cation-π stacking onto m^7G1639 in the last structure). The C-terminal region of 40S ribosomal protein RPS18/uS13 backbone is visible as a teal ribbon, mRNA trace is marked in yellow and 18S rRNA surface in grey.

Figure S8. Extended Figure 6.

(**A**) Complementary to Fig. 6B, the graph shows a correlation analysis between 5' UTR TE fold-change and Start TE fold-change, for all (blue), mitochondrial (red) and ribosomal (green) transcripts. The local regression fit (LOESS) is shown as line for each transcript group. Spearman correlation coefficient and p-value of correlation are given above, alongside number of transcripts used in the analysis. (**B**) As in (A) for correlation of 5' UTR TE fold-change and CDS TE fold-change. (**C**) As in (A) for correlation of Start TE fold-change and whole CDS TE fold-change. (**D**) As in (A) for correlation of Start TE fold-change and Start TE fold-change relative to whole CDS TE fold-change. (**E**) As in (A) for correlation of Start TE fold-change (ncorrected for CDS TE fold-change) and CDS TE fold-change. (**F**) Left panels: Metagene plot aligning ribosome footprint A-sites relative to coding sequence (CDS) around

start and stop codons, for Liv^{KO} (pink) and Liv^{WT} (dark green) for transcripts with specifically high (upper) and low (lower) GC content in 5' UTR. Right panels: Alignment of reads to the annotated transcriptional start site (TSS), and plotted separately for reads that fall into annotated 5' UTR (left) and CDS (right). Black line shows cumulative density of 5' UTRs (left) and CDS starts (right). (**G**) As in (F), but for transcripts with particularly long (upper) or short (lower) 5' UTRs according to the CAGE data. (**H**) Cross-correlation analysis between transcript sequence features considered in the analysis. (**I**) Linear regression model's prediction of TE FC variances explained by different transcript sequence features (color-coded; listed at bottom). TE FCs are predicted for 5' UTRs, CDSs and Start regions (first 20 codons, relative to whole CDS FCs). Total explained variance by a combination of transcript sequence features is given at the right of the bars. (**J**) Analysis of GC content within the 60 nt upstream of the initiation codon, for transcripts encoding mitochondrial proteins (red) vs. all transcripts (black), indicating no significant differences in GC-content in the mitochondrial group. In the upper part of the panel, the number of transcripts used for the analysis (n), their median (also shown as diamond symbol in graph) and the p-value for the difference from a ranksum test are given. (**K**) As in (J), for GC content of the full 5' UTR, for transcripts encoding mitochondrial proteins (red) vs. all transcripts (black). (**L**) As in (J), for Minimal Free Energy (MFE) of RNA folding in the window +/- 60 nt around the CDS initiation codon. (**M**) As in (J) for ATG count within the 5' UTR (and taking into account ribosome footprint coverage, serving as a proxy for AUG-initiated uORFs). (**N**) As in (M), but for alternative uORF start codons, (C/G/T)TG. (**O**) As in (J) for Kozak score. (**P**) As in (F), but for transcripts with particularly high (upper) or low (lower) GC content in the +60 nt region. (**Q**) Percentages of all (blue) and of mitochondrial protein transcripts (red) with G or C nucleotides at positions around the start and stop codons. A 10 nt moving window was used for averaging to smoothen the curves. It is evident that mitochondrial transcripts show higher GC content at the CDS beginning as compared to all transcripts.

Figure S9. Mendelian Randomization Analysis of Whole Blood METTL5 and TRMT112 Expression Across Cardiometabolic Traits and Tissues.

This figure presents Mendelian Randomization (MR) analyses examining the association of genetically predicted expression of METTL5 and TRMT112 in whole blood with cardiometabolic outcomes. (**A**) shows forest plots of MR estimates (Beta ± 95% CI) for METTL5 expression across primary and replication GWAS datasets. (**B**) presents the corresponding MR results for TRMT112. (**C**) displays a heatmap comparing the Z-scores (Beta/SE) for BUD23 across cardiometabolic tissues, including whole blood, subcutaneous and visceral adipose tissue, skeletal muscle, and heart atrial appendage. Asterisks (*) denote nominal significance ($P < 0.05$), and grey cells indicate unavailable instruments. (**D**) shows enrichment analyses for METTL5 and TRMT112, respectively, across predefined clinical categories in the Million Veteran Program (MVP). Bar heights reflect enrichment significance, and domains meeting Bonferroni or nominal thresholds are highlighted. All effect directions correspond to associations per increased gene expression in whole blood.